Photosynthesis Research
https://doi.org/10.1007/s11120-024-01117-2

RESEARCH

Insights from Ca^{2+}→Sr^{2+} substitution on the mechanism of O-O bond formation in photosystem II

Gabriel Bury[1] · **Yulia Pushkar**[1]

Received: 20 June 2024 / Accepted: 6 August 2024

Abstract
In recent years, there has been a steady interest in unraveling the intricate mechanistic details of water oxidation mechanism in photosynthesis. Despite the substantial progress made over several decades, a comprehensive understanding of the precise kinetics underlying O-O bond formation and subsequent evolution remains elusive. However, it is well-established that the oxygen evolving complex (OEC), specifically the $CaMn_4O_5$ cluster, plays a crucial role in O-O bond formation, undergoing a series of four oxidative events as it progresses through the S-states of the Kok cycle. To gain further insights into the OEC, researchers have explored the substitution of the Ca^{2+} cofactor with strontium (Sr), the sole atomic replacement capable of retaining oxygen-evolving activity. Empirical investigations utilizing spectroscopic techniques such as XAS, XRD, EPR, FTIR, and XANES have been conducted to probe the structural consequences of Ca^{2+}→Sr^{2+} substitution. In parallel, the development of DFT and QM/MM computational models has explored different oxidation and protonation states, as well as variations in ligand coordination at the catalytic center involving amino acid residues. In this review, we critically evaluate and integrate these computational and spectroscopic approaches, focusing on the structural and mechanistic implications of Ca^{2+}→Sr^{2+} substitution in PS II. We contribute DFT modelling and simulate EXAFS Fourier transforms of Sr-substituted OEC, analyzing promising structures of the S_3 state. Through the combination of computational modeling and spectroscopic investigations, valuable insights have been gained, developing a deeper understanding of the photosynthetic process.

Keywords Natural photosynthesis · Density functional theory · X-ray absorption spectroscopy · Electron paramagnetic spectroscopy · Water oxidation catalysis · Strontium

Abbreviations

AC	Acetate Ion, CH_3 COO^-
AO	Atomic Orbitaly
APS	Advanced Photon Source
CV	Cyclic Voltammetry
CW	Continuous Wave
DFT	Density Functional Theory
ENDOR	Electron-Nuclear Double Resonance
EPR	Electron Paramagnetic Resonance
ESEEM	Electron Spin-Echo Envelope Modulation
eV	Electron-Volts
EXAFS	Extended X-Ray Absorption Fine Structure
FTIR	Fourier-Transform Infrared Spectroscopy
LDAO	Lauryldimethylamine-N-Oxide
LHC	Light-Harvesting Complex
MLS	Multiline Signal
MS	Mass Spectroscopy
NMR	Nuclear Magnetic Resonance
O_2	Molecular Oxygen
OEC	Oxygen Evolving Complex
O-O	Oxygen-Oxygen bond
PCET	Proton-Coupled Electron Transfer
PS I	Photosystem I
PS II	Photosystem II
PY	Pyridine
RC	Radical Coupling
RR	Resonance Raman
Tyr_Z	Tyrosine Z
UV	Ultraviolet
WNA	Water Nucleophilic Attack

✉ Yulia Pushkar
ypushkar@purdue.edu

[1] Department of Physics and Astronomy, Purdue University, West Lafayette, IN 47907, USA

Published online: 26 August 2024

WOC	Water Oxidation Catalyst
WOR	Water Oxidation Reaction
XANES	X-Ray Absorption Near Edge Structure
XAS	X-ray Absorption Spectroscopy
XC	Exchange Correlation
XES	X-ray Emission Spectroscopy

Introduction

The oxygen-evolving activity of Photosystem II (PS II) protein plays a crucial role in sustaining the biosphere. Photosynthesis not only serves as the means to harvest light but also enables the conversion of sunlight into the chemical bonds of organic molecules – the fundamental building blocks of all living organisms – as well as oil, gas, and coal. PS II stands out as the sole known natural protein capable of evolving molecular oxygen from water. The photosynthetic process involves light capture and harvesting, as well as a complex electron transfer chain (Vinyard et al. 2013; Shevela et al. 2023) Reviews of the protein components in the photosynthetic process exist in the literature (Müh and Zouni 2020; Shevela et al. 2023). Central to the photosynthetic process is the oxygen evolving complex (OEC), which comprises an inorganic tetramanganese cluster, $CaMn_4O_5$, and serves as the driving force for the water-splitting reaction. The OEC undergoes a series of transformations referred to as the "Kok cycle," which involves five states, starting from the dark-adapted state (S_1) and progressing through intermediates S_1-S_0 (Kok et al. 1970). Over the past four decades, noteworthy progress has been made in understanding the structure-kinetics relationship in the OEC (Cox and Messinger 2013; Yano and Yachandra 2014; Klauss et al. 2015; Vogt et al. 2015b; Shevela et al. 2023). However, the critical step involving the formation of the O—O bond remains inadequately characterized. It is believed that O—O bond formation occurs on a microsecond to millisecond timescale during the S_3-to-S_0 step of the catalytic cycle, ultimately resulting in oxygen evolution, in large part due to the multitude of UV-Vis, and EPR, and other spectroscopy-based studies conducted in the 1980s and 1990s (Vrettos et al. 2001; McEvoy and Brudvig 2006); recent time-resolved works followed, yielding greater insight into the precise kinetics timescales, especially in this fast S_3-to-S_0 transition (Chukhutsina et al. 2019; Lubitz et al. 2019; Ibrahim et al. 2020; Poddar et al. 2022; Bhowmick et al. 2023; Greife et al. 2023). Despite ongoing efforts, directly monitoring this transient process has proven challenging, leaving many details yet to be fully elucidated.

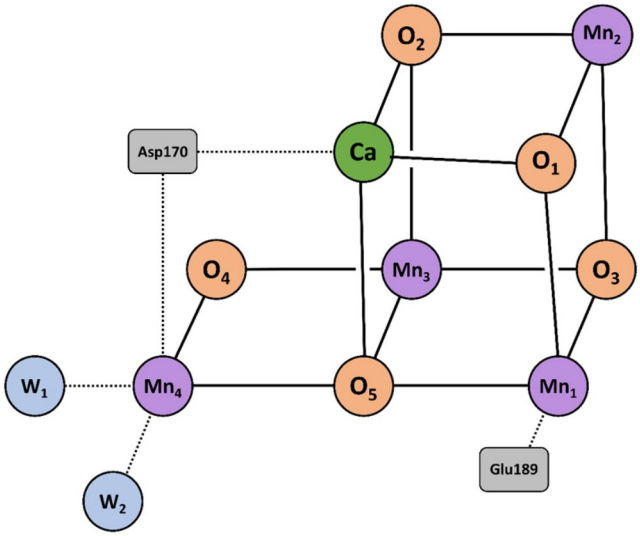

Fig. 1 The distorted "chair-like" cartoon image of the OEC, for use in establishing notation for atoms in the OEC, as well as identifying amino acids explicitly referenced in this work. W refers to a coordinating water molecule. The coordination of certain ligating amino acid residues is shown. Mn_4 is the "dangler" manganese in some models. Sr replaces Ca in Ca^{2+}→Sr^{2+} models, resulting in a slightly distorted structure. Mn_1, Mn_2, Mn_3, and Mn_4 are also referred to Mn_D, Mn_C, Mn_B, and Mn_A, respectively

The discovery of calcium as an indispensable cofactor in oxygen evolution marked a significant breakthrough in understanding the intricate structure of the oxygen-evolving complex (OEC), discovered independently in the same year by the Babcock/Yocum and Murata laboratories (Ghanotakis et al. 1984a; Miyao and Murata 1984). A single calcium ion is contained within each OEC unit – Fig. 1 provides a cartoon guide for notation of the atoms in the OEC, as well as of some ligating amino acids and water/oxo groups. Subsequent investigations demonstrated the proximity of this metal to the tetramanganese cluster, as evidenced by the detection (Boussac et al. 1989; Sivaraja et al. 1989) and subsequent characterization (Baumgarten et al. 1990; Boussac et al. 1990; Ono and Inoue 1990; Tso et al. 1991) of a long-lived modified electron paramagnetic resonance (EPR) multiline signal generated in the S_2 state of the calcium-depleted OEC. Further experimental techniques such as X-ray absorption spectroscopy (XAS) and pulsed EPR provided additional evidence supporting the presence of Ca^{2+} within the OEC; please refer to the EPR and XAS sections. Under normal catalytic conditions, $Tyr_Z^{\bullet}$ oxidizes the S_2 state to generate the S_3Tyr_Z state; however, calcium depletion prevents this reaction from occurring, obstructing the S-state cycle at the $S_2Tyr_Z^{\bullet}$ state. The underlying mechanism of this effect was initially suggested to be primarily electrostatic in nature. Given its vital role in driving S-state transitions and shaping the OEC structure, the calcium ion's significance has been extensively explored for several decades (Miqyass et al. 2008; Yocum 2008). A comparative analysis between OECs incorporating strontium (Sr) as a substitute for calcium and the native Ca OECs was performed. This work

presents an account of spectroscopic and computational investigations conducted on Sr-substituted PS II, highlighting significant disparities in the structure, function, and stability of OEC activity when compared to native (Ca) PS II. We contribute to the already discussed work with comparison of simulated EXAFS spectra produced from DFT-optimized structures of the S_3 state in CaOEC and SrOEC against experimentally derived EXAFS of deconvoluted S_3 states for both native and SrOEC.

Preparation of SrOEC

Early methods for achieving Sr-PS II include Sr reconstitution of Ca^{2+}-depleted PS II centers. Ghanotakis et al. reported a protocol for inhibiting the oxygen-evolving activity of PS II (Ghanotakis et al. 1984). Purified PS II complexes were exposed to a salt treatment, releasing two water-soluble polypeptides (23 and 17 kDa) (Ghanotakis et al. 1984a, b). Such procedures to remove Ca^{2+} were found to lead to inhibition of a small proportion of PS II centers (Shen and Katoh 1991; Boussac and Rutherford 1995). Following Ca depletion, reconstitution with Sr^{2+} can be achieved with incubation in a Sr-based buffer (Boussac et al. 2000, 2004) or simply by cyanobacterial growth in a Sr-based buffer. Reports in the mid-1980s discover that following NaCl washing, Ca^{2+} release is a light-dependent process (Dekker et al. 1984; Miyao and Murata 1986). In 2004, Boussac et al. reported a method for isolating the Sr^{2+}/Ca^{2+}-containing thylakoid and PS II core complexes formed from *Thermosynechococcus elongatus* based on previously established methods for thylakoid preparation, with minor modifications (Sugiura and Inoue 1999). Other similar methods for growth of *T. elongatus* with Sr substitution have been reported (Suzuki et al. 2006; Gates et al. 2016).

Functional effects of Sr substitution

In 1984, the laboratory of Babcock and Yocum demonstrated that the addition of small quantities of Ca cation restores oxygen-evolving activity in PS II prepared in high concentrations of NaCl; however, they note that Sr^{2+}, alongside other cations, is also able to restore lost oxygen-evolving activity, though not as completely (Ghanotakis et al. 1984). Later works by Boussac and Rutherford reported similar reductions in oxygen-evolution rates with Sr substitution preparations, alongside EPR analysis suggesting a slowing of the S_3-to-S_0 transition (Boussac and Rutherford 1988, 2000; Boussac et al. 1992).

An EPR-based study (Boussac et al. 2004), addressed later in greater detail, demonstrates that Sr PS II has increased stability of the S_3 state, alongside increased rates of electron donation from Tyr_D and an increased rate of oxidation from $S_0 \rightarrow S_1$ by Tyr_D. Slowed kinetics consistent with the rate of $S_3Tyr_Z^{\cdot}$ to S_0Tyr_Z transition suggests Tyr_Z redox acts as a rate-limiting step in Ca/Sr enzymes. Later work suggests this slowdown is a function of entropic change with Sr substitution perturbing the hydrogen bonding network about Tyr_Z (Rappaport et al. 2011); this is later supported with water-exchange experiments performed by (Nilsson et al. 2014), highlighting the need for a highly ordered hydrogen-bonding water network for low-energy O-O bond formation.

Ishida et al. (Ishida et al. 2008) studied the roles and importance of the Ca^{2+} and Cl^- cofactors in oxygen-evolving activity of *T. elongatus* with Sr^{2+} and Br^- substitution, respectively; this study yielded 4 different enzymes: Ca/Cl, Ca/Br, Sr/Cl, and Sr/Br. Four groups of wild type cells were grown under previously reported conditions (Sugiura et al. 2004) and were uniquely supplemented with 0.8mM YX_2 buffer (Y = Ca or Sr; X = Cl or Br). It was determined that the effects of Ca^{2+} to Sr^{2+} and Cl^- to Br^- substitution are additive, and the effect of Ca^{2+} to Sr^2 substitution is greater than the effect of the Cl^- to Br^- substitution. This is due to the perturbation of the OEC cubane structure with the larger ionic radius of Sr^{2+} compared to Ca^{2+}. Absorption changes at 292 nm were observed for each of the four enzymes, after flashes in a series 400 ms apart – enabling reduction of the Tyr_Z radical by the Mn_4Ca/Sr cluster. Neither Sr^{2+} nor Br^- substitution lead to worsened turnover rate in the S-state cycle under the flashing conditions. This contrasts with the substantial decrease in oxygen evolution activity under steady-state conditions. Thus, Ishida et al. conclude a decreased efficiency of the cycle results due to an intrinsic change in kinetics in the cycle, as opposed to an increase in the number of inactive PS II centers.

Alongside the crystal structure on Sr-substituted PS II derived from *T. vulcanus*, Koua et al. analyzed the oxygen-evolving activity of the Sr-substituted photosynthetic protein (Koua et al. 2013), with an oxygen evolving rate of 46% the rate of native PS II. A rate of 3750 µmol O_2/mg chl a/hr is reported for non-crystallized Ca-PS II, whereas Sr-substituted activity is reduced by a third (63% activity).

Gates et al. (Gates et al. 2016) perform oxygen-evolution studies on whole cells of *T. elongatus* replaced with strontium. They report lower rates of oxygen release, in line with previous reports. They highlight a higher Arrhenius activation barrier for O_2 evolution associated with Sr-substituted *T. elongatus* cells compared to the Ca-based native. They observe that for PS II-WO (Sr), flux through the Q_AQ_B acceptor gate acts as the limiting process for turnover rate

in vivo. As such, they introduce benzoquinone derivatives binding the Q_B site and removing this kinetic inefficiency. This results in a 31% *higher* yield for Sr-substituted PS II-WOC compared to the native Ca. This effect is particularly observed at low light conditions, with fewer backward transitions and a longer lifetime of the unstable S_3 state, posited to be an effect of the stabilization of the Sr-WOC compared to the photoactive Tyr_z. At higher temperature (~45 °C), the greater activity of PS II centers in Sr-grown cells is responded with a reduced number of active PS II-WOC/Chl, resulting in comparable oxygen-evolution activity per cell.

Structural and spectroscopic analysis of SrOEC

XRD

Recent reviews (Cox et al. 2020; Simon et al. 2023) highlight the progress in crystallographic methods on PS II with the improvement of free-electron laser sources. In 2011, Umena et al. acquired a 1.9 Å structure (Umena et al. 2011) of purified PS II core complexes from thermophilic cyanobacterium, *T. vulcanus.* This resolution is an improvement upon prior solved structures on PS II, including work on closely related *T. elongatus.* The electron density mapping from Umena et al. (1.9 Å structure) located the metal atoms of the cubane Mn_4CaO_5 cluster alongside all ligands. This structure identified more than 1300 water molecules in each photosystem II monomer, identifying extensive hydrogen-bonding networks able to serve as channels for protons, H_2O, or oxygen molecules. Subsequently, in 2013, Koua et al. published a 2.1 Å structure of Sr-substituted PS II derived from *T. vulcanus* and compared the structure to the 1.9 Å structure of Ca PS II obtained years prior. The occupancy of Sr atoms in the structure was ~0.7 and resulted in a lower electron density of Sr^{2+} compared to that of the Mn ions, consistent with prior reports of reduced Sr^{2+} occupation in Sr^{2+} PS II (Strickler et al. 2005; Boussac et al. 2008; Yano et al. 2011). Coupled to the lower occupancy of the Sr^{2+} ion is the lowered occupancy of the W3 and W4 water molecules, themselves associated with Ca/Sr, though the accuracy of their position in the mapping is unaffected. Subsequent XFEL-based structures on Ca PS II (Kern et al. 2018; Suga et al. 2019) obtained with low X-ray induced damage have shown similar structure as reported by Umena et al.

Mn-Mn and Sr-Mn distances of key XRD structures are summarized in Tables 1 and S1. Table 1 shows that the relative positions of the four Mn ions are similar in both Ca and Sr PS II. The average Mn_1-Mn_4 distance, 0.1 Å longer for Sr, and the average Mn_3-Mn_4 distance, 0.1 Å shorter for Sr, differ from the native Mn_4CaO_5 cluster. Please note that these distances might also be affected by variable X-ray dose in two XRD experiments which can result in variable content of photo-reduced Mn centers. Photo-reduction of Mn centers typically increase Mn-Mn distances. DFT modeling (see below and in Table S2) shown elongation of some Mn-Mn distances in Sr based OEC models in agreement with XRD results. More substantial than the slight variations in locations of the Mn ions is the positioning of the Sr^{2+} ion, located more toward the outside of the cubane. The displacements of the Ca and Sr ions in the monomers of each structure, due to conformational changes with Sr substitution average to be 0.3 Å. The resulting distorted Sr-cubane structure yielded Sr-Mn distances ~0.2 Å greater than analogous distances for native Ca-Mn distances. These elongations may be in part attributed to a larger ionic radius

Table 1 Distances between Ca/Sr–Mn, Mn–Mn, and Ca/Sr–O atoms. The distances are taken as average of the two monomers. All structures are of the dark-stable S_1 state, either from XRD or XFEL methods

	1.9 Å, Ca PS II (Umena et al. 2011)*	2.0 Å, Ca PS II XFEL (Kern et al. 2018)	2.05 Å Ca PS II XFEL (Suga et al. 2019)	2.1 Å, Sr PS II (Koua et al. 2013)*
Ca/Sr – Mn_1	3.52	3.43	3.61	3.55
Ca/Sr – Mn_2	3.34	3.38	3.42	3.50
Ca/Sr – Mn_3	3.42	3.51	3.40	3.64
Ca/Sr – Mn_4	3.80	3.83	3.75	4.00
Mn_1 – Mn_2	2.82	2.78	2.59	2.78
Mn_1 – Mn_3	3.28	3.24	3.16	3.34
Mn_1 – Mn_4	4.95	4.85	4.96	5.06
Mn_2 – Mn_3	2.90	2.85	2.72	2.92
Mn_2 – Mn_4	5.41	5.20	5.27	5.42
Mn_3 – Mn_4	2.93	2.74	2.89	2.88
Ca/Sr – O_1	2.41	2.30	2.58	2.44
Ca/Sr – O_2	2.51	2.48	2.64	2.66
Ca/Sr – O_3	3.91	3.78	4.16	3.99
Ca/Sr – O_4	3.98	4.19	3.82	4.03
Ca/Sr – O_5	2.50	2.56	2.59	2.59

* Please note that these distances might also be affected by variable X-ray dose in two XRD experiments which can result in variable content of photo-reduced Mn centers. Photo-reduction of Mn centers typically increase Mn-Mn distances

of Sr^{2+} compared to Ca^{2+} (0.99 Å to 1.12 Å, with Ca→ Sr substitution). Thorough analysis of the differences in oxo-bridging oxygens is hampered by the lower electron densities of the oxygens compared to Mn and Ca/Sr and by the reduced occupancy of the Sr^{2+} ions. These factors yielded higher experimental errors for these distances. Given that the Mn-O distances between both structures differed on average by 0.1–0.2 Å and that some of these bonds are shorter while others are longer in the Sr-based structure, at least some of these differences can be attributed to experimental error.

XAS

While early XRD-derived structures were able to locate the electron density associated with the Mn_4Ca cluster within the PS II complex, they were limited by resolution (3.2–3.5 Å) (Zouni et al. 2001; Kamiya and Shen 2003; Biesiadka et al. 2004; Ferreira et al. 2004). As such, detailed structures critically depended on input from a variety of spectroscopic techniques to acquire an accurate determination of positions of the Mn/Ca and bridging/terminal ligand atoms. Early Mn (Yano et al. 2005b) and Ca (Cinco et al. 2002) K-edge XANES and EXAFS studies were able to more precisely deduce Mn-Mn/Ca/ligand distances due to the then-limiting levels of X-ray doses used in XRD. PS II crystals of the Mn_4Ca cluster were highly susceptible to radiation damage, and with the lower X-ray doses required for EXAFS/XANES experiments, any radiation damage could be precisely monitored and controlled. Many works (Dau et al. 2004; Yano et al. 2005a; Grabolle et al. 2006) warn of the potential to reduce $Mn^{III/IV}$ to Mn^{II} at sufficiently high X-ray doses and temperatures.

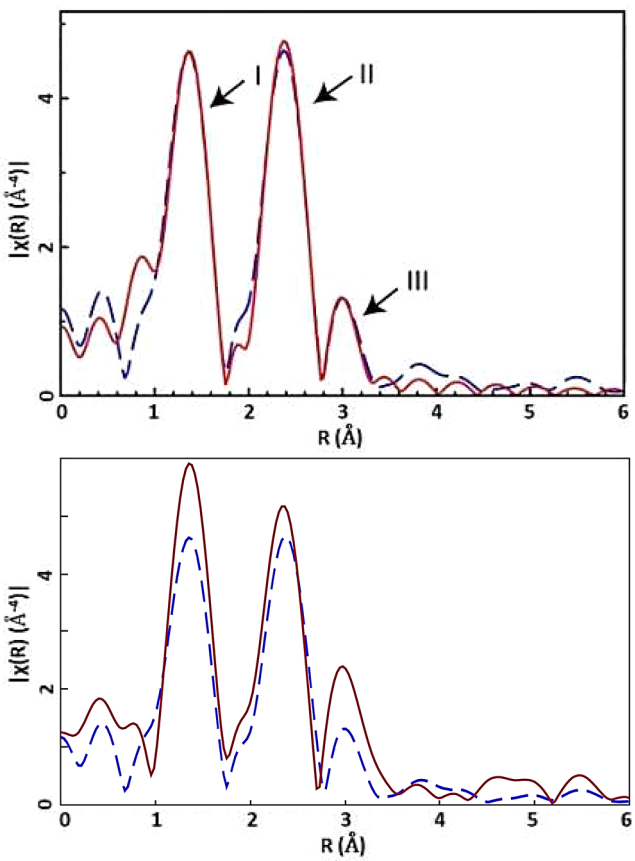

Fig. 2 **a**) Overlays of Fourier transforms, k = 4-11.45Å, of EXAFS data for native OEC from spinach prepared in the dark-stable S1 state. Red: Fourier transform of room-temperature EXAFS collected by Davis et al. 2015 at APS (Davis and Pushkar 2015). Blue: EXAFS fit produced by Davis et al. revealing Mn coordination environment in agreement with prior cryogenic XAS and XRD structures. Characteristic peaks I, II, and III are indicated with arrows. **b**) SrOEC data from T. elongatus (Pushkar et al. 2008), red, are compared to the same CaOEC data from spinach, blue. Increase in the peak III intensity is due to stronger Mn-Sr scattering

Cinco et al. performed a Ca EXAFS-based study (Cinco et al. 2002) on native PS II membrane fragments, prepared as BBY particles from spinach. Fourier transforms of their Ca EXAFS from active (Chelex-treated samples) revealed an inner coordination shell, described by 5–6 O atoms at 2.4 Å. Another significant peak in their Fourier transforms was fitted to a Ca-Mn coordination at 3.4 Å. Note that these samples are characterized by 2 Ca/PS II, due to the presence of one calcium in both the OEC (Mn cluster) and the light-harvesting complex II (LHC II). Recently Ca valence-to-core X-ray emission spectroscopy was proposed as an additional tool for analysis of the Ca ligand environments (Mathe et al. 2019). In 2005, Yano et al. through Mn EXAFS, refined existing structures of the Mn-OEC. They revealed three short Mn-Mn distances, between 2.7 Å and 2.8 Å and resultingly, the same number of di-μ-oxo-bridging units as well; prior works (Hasegawa et al. 1999; Dau et al. 2001; Robblee et al. 2002) were not able to determine whether there are two or three di-μ-oxo-bridged Mn-Mn moieties, due in part to the inherent error of EXAFS methods in determining the number of Mn-Mn vectors (Yachandra 1995). These insights provided much-needed clear limitations on the proposed structures based on prior spectroscopic and diffraction data for native PS II.

One EXAFS study on native PS II at room-temperature was performed by Davis et al. in 2015 (Davis and Pushkar 2015). Their single shell analysis of the first coordination sphere (Mn-O interactions) fit the data to three Mn-O interactions at 1.9 Å; later fits refined this to two Mn-O interactions at 1.82 Å and one Mn-O interaction at 1.99 Å. Analysis of peak III of the Fourier transform – shown in Fig. 2 – is challenging due to a low intensity and contributions from multiple absorber-backscatterers: Mn, Ca, and C.

Having considered EXAFS of native PS II, we can consider the work done on Sr-substituted PS II. Pushkar et al. (Pushkar et al. 2008) perform an EXAFS-based study on *T. elongatus* prepared as CaPS II and exchanged Sr PS II.

Samples are advanced through the S-state cycle via consecutive laser flashes followed by immediate freezing in liquid nitrogen (Messinger et al. 2001). Mn K-edge EXAFS spectra are obtained for both native PS II and the Sr-substituted PS II for subsequent flashes, corresponding to structures in the S_1, S_2, S_3, and S_0 states, cyclically. Mn K-edge EXAFS data ensure the integrity of the samples and the absence of radiation damage to the core structure of the Mn_4 core. Fourier transforms (FT) of the Mn EXAFS data reveal three major peaks: I, characteristic of the 1.8 Å Mn-oxo bridging ligand distances, II, characteristic to 2–3 di-μ-oxo-bridged Mn-Mn interactions ~ 2.7 Å, and III, characteristic of one mono-μ-oxo-bridged Mn-Mn and from Mn-Sr interactions. While EXAFS of the S_1, S_2, and S_0 states are similar, peaks II and III are attenuated and lowered in intensity for the S_3 state. This suggests structural changes in the OEC in the S_3 state. Figure 2 shows Fourier transforms of CaOEC showing the three characteristic peaks.

Sr EXAFS are more informative and can more clearly resolve Sr-Mn interactions in all S states. Sr XANES spectra (Pushkar et al. 2008) reveal differences in the S-state spectra and the spectrum of hydroxylamine-inhibited (HYD) "inactive" Sr-PS II, revealing a different first coordination environment for Sr in active PS II and from free ion Sr^{2+}; FT of the HYD spectra reveal no peak II, associated with Sr-Mn interactions. The analogous peak I for Sr EXAFS suggests one shell of 7–8 oxygen atoms ~ 2.5 Å, while the FT peak II corresponds to two different Sr-Mn interactions for all S states. Sr-Mn interactions are fitted at ~ 3.5 Å and ~ 4.0 Å for all S-states in Sr. Prior Ca EXAFS of native (Cinco et al. 2004) PS II and Sr EXAFS of Sr-reactivated PS II membranes (Cinco et al. 1998) indicated proximity of the Ca at 3.4 Å and Sr at 3.5 Å to the Mn cluster in the S_1 dark-stable state of the OEC. The work of Pushkar et al. unambiguously demonstrated that Sr is proximate to the OEC in all S states with significant changes in Sr(Ca)–Mn interactions with sequential flashes – as the enzyme proceeds through the catalytic cycle.

Now addressing XANES spectra, we revisit the work done on Sr-substituted PS II. Pushkar et al. (2008) perform an EXAFS-based study on *T. elongatus* prepared with native Ca and biosynthetically exchanged Sr-PS II preparations (Boussac et al. 2004). Having discussed Mn EXAFS previously, we can discuss the results of Sr XANES which can more clearly resolve Sr-Mn interactions in all S states. Sr XANES spectra (Pushkar et al. 2008) reveal differences in the S-state spectra and the spectrum of hydroxylamine-inhibited (HYD) "inactive" Sr-PS II. This indicated that the first coordination environment about Sr in active PS II differs from that of free Sr^{2+} – Fourier transforms of HYD Sr-PS II spectra did not show a peak assigned to Sr-Mn interactions for active Sr PS II. In the same work, examination of Sr PS II Mn XANES revealed a shift in the Mn K-edge between the S_1 and S_2 states consistent with the oxidation of the Mn core. A much more minor shift occurs between S_2 and S_3. However, with a third flash, the edge position restores to a lower energy from the S_3-to-S_0 spectra, expected with Mn reduction. The observation of Mn K-edge shifts from S_1-S_3 was further evidencing the $Mn^{III}{}_2Mn^{IV}{}_2$ S_1 oxidation state and Mn-oxidation with advancement S-states, for both Ca and Sr PS II.

EPR

When illuminated at 195 K by visible light for 5–10 min, native PS II advances to low-spin isoform of the S_2 state (S_{total}=½, with Mn^{III}/Mn^{IV} and Mn^{IV}/Mn^{IV} antiferromagnetically coupled), characterized by the so-called multiline signal (MLS). This feature is characterized by at least eighteen partially resolved hyperfine lines near g-factor 2. There exists substantial evidence of a spin isomorphism in the S_2 state, with a high-spin (S = 5/2) and a low-spin (S = 1/2) form, which have been characterized by EPR spectroscopy. The low-spin (S = 1/2) isoform of the S_2 state is often obtained by illumination at 195 K, with use of a heat/IR filter; illumination times are dependent upon the intensity of the light source. The low spin to high spin transition occurs with absorption of ~ 820 nm (IR) light. IR illumination at decreasing temperatures (170 K → 65 K) produces more of the high-spin state, as observed through the g = 4.1 signal in EPR spectroscopy (Boussac et al. 1996, 1998). The high-spin state may be converted back to the low-spin state by annealing (~ 200 K) in the dark. The presence of certain cryoprotectants, such as glycerol and ethylene glycol, have been shown to inhibit the formation of the high-spin S_2 state (Zimmermann and Rutherford 1986; de Paula et al. 1987); sucrose, however, is a cryoprotectant allows for formation of either the high-spin or low-spin S_2 state. It has been demonstrated that following NaCl washing, Sr^{2+}-reconstituted PS II demonstrates the high-spin g = 4 state is more easily reproduced than with Ca^{2+} reconstitution, when both samples are illuminated for 5 min at 200 K (Boussac and Rutherford 1988). Figure 3 summarizes the S_2 state isomorphism.

Kim et al. (2004) performed X-band CW and ESEEM spectroscopy studies on Ca^{2+} and Sr^{2+} reconstituted PS II. The already characterized (Boussac and Rutherford 1988) $S_2Tyr_Z^{\bullet}$ split signal was reproduced to confirm Ca^{2+} depletion in all sample preparations. The Ca^{2+}-reconstituted sample was found to be nearly identical to the native PS II MLS, while the Sr^{2+}-reconstituted sample showed a significantly altered MLS, featuring narrower hyperfine splitting and a different intensity pattern compared to the control samples; which were reproduced (Boussac et al. 2004). Three-pulse ^{87}Sr ESEEM was used to probe the Mn cluster-Sr/

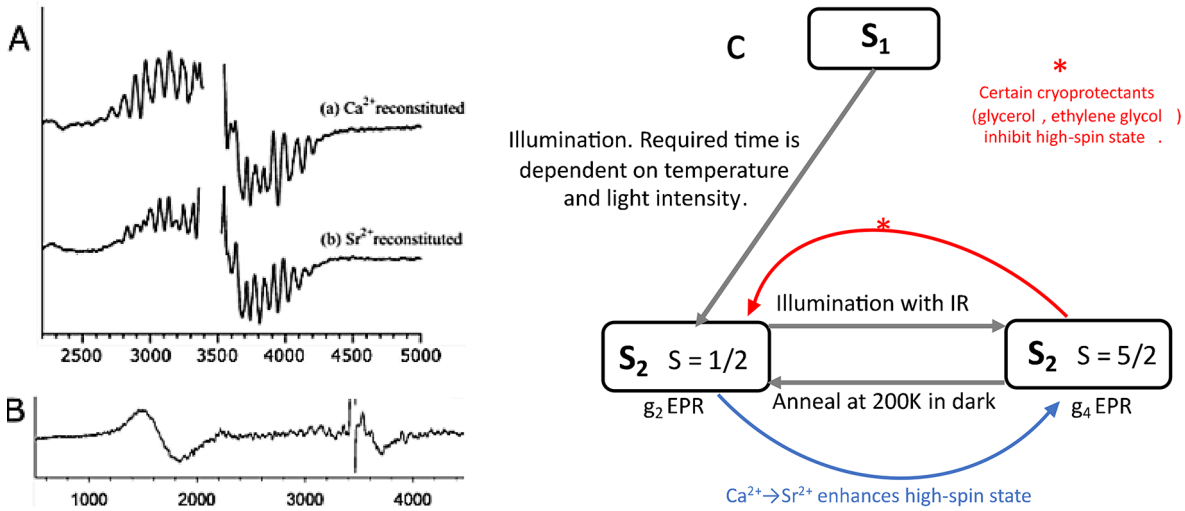

Fig. 3 Description of fundamental EPR features to PS II. **a**) A description of the effect of Ca^{2+}→Sr^{2+} substitution on the multiline signal (MLS) in the S_2 state, the characteristic EPR feature of the low-spin (S = 1/2) isoform appearing near g-factor 2. Adapted from (Kim et al. 2004). **b**) Depiction of the g = 4.1 feature resulting from the high-spin (S = 5/2) isoform of PS II. Adapted from (Haddy et al. 2004). **c**) A scheme for the formation and conversion between states of the high-spin and low-spin isoforms of the S_2 state

Ca distances (Kim et al. 2004). While three-pulse ESEEM of the natural abundance (7% abundance ^{87}Sr) Sr sample exhibited no modulation, ^{87}Sr-enriched samples revealed a clear modulation from the spin = 9/2 ^{87}Sr nucleus, weakly magnetically coupled to the Mn cluster. With a point dipole approximation for electron spin, they concluded a Mn-Ca/Sr distance in the 3.8-5.0 Å. This early ^{87}Sr ESEEM approach provided independent evidence contemporary with XAS experiments, suggesting that the Ca/Sr binding site is close to the Mn cluster in the OEC of PS II.

Cox et al. (Cox et al. 2011) produced ^{55}Mn ENDOR spectra of Ca and Sr OEC prepared in the S_2 state, B_0 = 1260 mT. Contrasting CW X-band and ESE Q-band spectra, the Ca and Sr OEC produce comparable results for ^{55}Mn-ENDOR spectra; both display a similar total spectra breadth (60–200 MHz). Approximately six ENDOR peaks are resolved for both Ca^{2+} and Sr^{2+} variants of the OEC, with only minor changes in the line intensity of the peaks. Of the six peaks, only the first two demonstrate a minor downshift in position, by approximately 10 MHz. Comparing ^{55}Mn-ENDOR spectra from *T. elongatus* with data from spinach, differences intrinsic to species have a larger effect on the spectra than does Ca^{2+}-to-Sr^{2+} replacement (Kulik et al. 2005a, b). The change in CW spectra with Ca^{2+}→Sr^{2+} replacement is due to a decrease in the hyperfine tensor anisotropy. Some prior DFT-based models (Pantazis et al. 2009; Siegbahn 2009) were found to be consistent with the data presented by Cox et al. positing a 5-coordinate Mn^{III} as a site for substrate water binding.

The Mülheim group (Rapatskiy et al. 2012; Pérez Navarro et al. 2013; Lohmiller et al. 2014) explored the use of ELDOR-Detected NMR (EDNMR) for use to study the PS II OEC complex. W-band ^{17}O-EDNMR experiments shifted the resonant side bands out of the main EPR region. PS II (75% isotope enrichment) flashed into the S_2 state, gave ^{17}O resonances for three distinct oxygens coordinating the Mn_4O_5Ca cluster. The largest couplings appeared from the O_5 bridge and two waters bound to Ca and Mn_4. A doublet assigned to a μ-oxo bridge revealed sensitivity to Ca/Sr exchange (~5% change in splitting), as well as NH_3 binding (displacing W1, 30% shift). X-band CW EPR spectra of the Sr^{2+}-substituted S_2 state in PS II samples with and without $H_2{}^{17}O$ indicate no line broadening upon ^{17}O exchange. The lack of line broadening with ^{17}O exchange demonstrates that the largest ^{17}O coupling represents only one exchangeable oxo bridge. A recent TR-MIMS and TR-EDNMR approach (de Lichtenberg et al. 2024) identified the central oxygen bridge, O_5 as having the same exchange rate as the substrate water W_S; these rates were also shown to be similarly affected by Ca^{2+} → Sr^{2+} exchange, suggesting O_5 fulfills all criteria for being the substate water.

In 2017, Guo et al. (Guo and Barry 2017) conducted a study on the effect of Sr substitution on the $Tyr_Z^{\bullet}$ decay rate and PCET by monitoring the $Tyr_Z^{\bullet}$ EPR signal intensity as a function of time, when the S_2 state was trapped by illumination at 190 K. At pH 7.5, Sr-substituted PS II results in a $Tyr_Z^{\bullet}$ decay rate which is decreased relative to the decay rate for native Ca PS II. However, at pH 6.0, the $Tyr_Z^{\bullet}$ decay rate is unaffected by Sr substitution. A two-pathway model was proposed to explain these results and is consistent with evidence towards a functional interaction of an S_2 protonated water cluster and Tyr_Z proton donation pathway.

In 2015, Boussac and coworkers (Boussac et al. 2015) demonstrated that Ca^{2+}→Sr^{2+} exchange in *T. elongatus*

perturbs proportions of OECs showing high (5/2) versus low-spin (1/2) S_2 states. Different illumination conditions – a single laser flash at room temperature versus illumination at 198 K – were shown to produce distinct EPR signals associated with the S_2 state; 1 flash produces an Sr-MLS alongside an S = 5/2 feature at g-factor 4.9. Illumination at 198 K reveals similar levels of the MLS signals alongside a distinct S = 5/2 feature: at g-factor 4.3. That annealing the 198 K-illuminated sample converted the g ~ 4.3 signal to the 4.98 signal suggests an equilibrium between these heterogeneous states at higher temperatures not observed at 198 K. Twice-flashed samples revealed a characteristic S = 3, g-factor 9.5 feature of the S_3 state alongside a reduction in the Sr-MLS feature, consistent with their miss-factor. On the other hand, once-flashed (room temperature) then 198 K-illuminated samples showed similar levels of the g-factor 9.5 S_3 state feature, alongside a reduction in the g-factor 4.9 feature with no change to the Sr-MLS. Similarly, as was observed in the S_2 states, annealing of the "once-flashed (RT), then-illuminated (198K)" sample produced g-factor 4.9 signal, at a reduction in the Sr-MLS intensity. These results suggest that S = 5/2 S_2 state centers advanced to S_3 at 198 K, while S = 1/2 S_2 states could not.

Beal et al. (Beal et al. 2018) considered the S_2, $S_2Tyr_Z^{\bullet}$, and S_3 state of the OEC for Ca and Sr-substituted forms via a BS-DFT study. Computed tyrosyl radical g-tensors and ^1H hyperfine couplings for the Ca PS II form found good agreement with prior EPR experiments (Sanakis et al. 2008; Boussac et al. 2009). Difference in the calculated g-tensor for the tyrosyl radical with Sr substitution was attributed to changes in the hydrogen-bonding environment in $S_2Tyr_Z^{\bullet}$ caused by the presence of Sr. Modelling of the S_3-peroxo state for Ca PS II resulted in a change in ligation for Ca in the S_2-S_3 transition; W_3 originally bound to Ca was found to deprotonate and migrate to a vacant adjacent Mn site. However, in Sr-substituted models, this spontaneous migration was not found to occur. Beal et al. went on to suggest that this deprotonation-migration response, leading to a difference in the coordination environment of the heterocation, is a substantial factor leading to the decrease in oxygen-evolving activity for Sr-substituted PS II.

A later work by Boussac and coworkers (Boussac et al. 2018) revealed that the S_2^{LS} and S_2^{HS} states' equilibrium is pH dependent, with pK_a of 8.3 for CaOEC and 7.5 for SrOEC. Subsequent DFT study revealed Ca→Sr exchange modifies electronic structure of indirect ligands to the heterocation; several groups within the active site such as W1, W2, Asp61, His332, and His337 showed changes in electronic structure – observed by a change in charge density – consistent with modification of the pK_a with heterocation exchange. Addition of ammonia reversed the effect of high pH, leading to a detectable NH_3-S_2^{LS} being present for all studied pH values, though NH_3 binding is not present in the $S_3Tyr_Z^{\bullet}$ state. That S_2^{HS} is observed to advance to S_3 at 198 K, while S_2^{LS} advances only at 240 K and above provided strong experimental support for theoretical studies (Bovi et al. 2013; Retegan et al. 2014; Ugur et al. 2016) suggesting S_2^{HS} is an intermediate in S_3 formation. Molecular interpretation of the S_2^{HS} given by our group as an early substrate binding state with Mn_1-OH fragment agrees with this overall conclusion (Pushkar et al. 2019).

FTIR

In an FTIR report by Chu et al. (Chu et al. 2000), a Mn-O-Mn vibrational mode in the S_2 state at 606 cm^{-1} was revealed and characterized. The corresponding Mn-O-Mn mode in the S_1 state was identified at 625 cm^{-1}. This band, through sensitive to ^{18}O substitution, is unaffected by D_2O or $^{44}Ca \rightarrow {}^{40}Ca$ substitution. Substitution of $Ca^{2+} \rightarrow Sr^{2+}$ upshifted this S_2 606 cm^{-1} band to 618 cm^{-1}, indicating that this oxo interacts with the Ca^{2+}/Sr^{2+} in the OEC. A C = O stretching mode of protonated carboxylic acid can be expected in the 1700–1750 cm^{-1} region, and in the S_2-minus-S_1 difference spectrum of wild type *Synechocystis* PCC 6803, many such bands appear (Pokhrel and Brudvig 2014). One such band appears at 1747 cm^{-1} and is sensitive to the presence of D_2O; $Ca^{2+} \rightarrow Sr^{2+}$ substitution results in the disappearance of this band (Strickler et al. 2005; Service et al. 2010). A work featuring flash-induced FTIR difference spectroscopy considered difference spectra of four S-state transitions – $S_1 \rightarrow S_2$, $S_2 \rightarrow S_3$, $S_3 \rightarrow S_0$, and $S_0 \rightarrow S_1$ – on flashed core PS II complexes from spinach and *T. elongatus*, both with Ca^{2+} and with Sr^{2+} substitution (Suzuki et al. 2006). This work observed significant intensity changes in symmetric COO^- peaks at the first and third flashes, leading to the conclusion that three carboxylate ligands are perturbed by $Ca^{2+} \rightarrow Sr^{2+}$ exchange. These data and prior mutagenesis works suggest these carboxylate groups ligate the Mn ions and are strongly coupled to the heterocation, rather than directly ligating the Ca^{2+}/Sr^{2+}. A 2017 work by Kim and Debus (Kim and Debus 2017) revealed that the Ca^{2+}-bound W_3 water molecule acts as the second substrate water molecule. The deprotonated form of W_3 moves adjacent to O_5 with the $S_2 \rightarrow S_3$ transition. Their work, through FTIR difference spectroscopy with $Ca^{2+} \rightarrow Sr^{2+}$ substitution, revealed a singular water molecule whose D-O-D bending mode is eliminated immediately prior to O-O bond formation. A similar FTIR work was published in 2018 by Guo et al. (Guo et al. 2018) This report included a description of two CO stretching bands (1503 cm^{-1} and 1478 cm^{-1}) present in calcium-containing PS II in the S_2 state trapped by illumination. They reveal a minor upshift in the 1503 cm^{-1} band to 1507 cm^{-1} for Sr-substituted PS II – a band which

is greatly reduced in Ca-depleted PS II. This result is consistent with the existence of a hydrogen-bonding interaction network between the Ca site and the $Tyr_Z^{\bullet}$.

Computational modelling

SrOEC

Many older computational models of the Sr-substituted OEC were based on the early 3.5Å XRD structure produced by Ferreira et al. (Ferreira et al. 2004). The 2004 structure was an improvement over the first X-ray structure, obtained at 3.8 Å resolution for PS II isolated from the cyanobacterium *T. elongatus* by Zouni et al. (Zouni et al. 2001). A review by Gerey et al. (Gerey et al. 2016) discusses the role and history of Mn-Ca/Sr heterometallic compounds and their use in model study of the OEC of PS II. They note that the first Mn-Ca compound was published in 2000, followed five years later by discrete Mn-Ca and Mn-Sr compounds. As such, the emergence of higher-resolution XRD structures – both of native CaOEC and SrOEC – were vital to the development of sound computational models. Our focus will be on the more modern work that has found sufficient experimental support with spectroscopic methods.

One influential report (Siegbahn 2009) by Siegbahn drastically improved the level of detail of study of the active site by presenting a model size of 170 atoms – larger than used in previous computational studies – and found good agreement with available experimental spectroscopic evidence. The structures presented were based in part on two models: the aforementioned 3.5Å model presented by Ferreira et al. (Ferreira et al. 2004), as well as the more recent 3.0Å model reported by Loll et al. (Loll et al. 2005). This report, alongside prior computational work (Siegbahn 2008) on modelling the OEC, revealed that an oxygen radical preceded O-O bond formation – previous attempts to model water nucleophilic attack on Mn-oxo groups consistently led to substantial barriers (Siegbahn and Crabtree 1999). As such, the search for effective O-O bond mechanisms was conducted via exploring all possible O-O bonds in the most promising S_4 state structures (Siegbahn 2006). The structures produced by Siegbahn resembled a slightly distorted version of the London model (3.5 Å) (Ferreira et al. 2004; Sproviero et al. 2008). Subsequent addition of protons and electrons led to the lower S-state structures, with later optimizations achieving structures consistent with available XAS experiments, (Liang et al. 2000; Haumann et al. 2005), with shorter Mn-Mn distances to the dangling manganese (Mn_4), as well as a reconstruction and rearrangement of the OEC in the $S_2 \rightarrow S_3$ transition. The structural rearrangement, motivated by the binding of a second substrate water, occurs alongside oxidation of Mn_2 from Mn^{III} to Mn^{IV}; with the binding of a water molecule to the dangler manganese, it becomes 7-coordinated, leading to a transfer of O_5 oxygen to Mn_1, becoming 6-coordinated alongside its oxidation, Fig. 4a. With the loss of a proton to the protein environment, this rearrangement becomes feasible and substantially smaller than in previously reported models: Mn_1 moves by 0.4Å, and all other metal atoms move by less than 0.2 Å. Despite this smaller-scale reconstruction of the OEC, it resulted in a higher energy of the S_3 state – already uphill – by 3 kcal/mol (0.13 eV). This energetic issue was resolved with a rearrangement of Glu189. Originally, Glu189 bridged Mn_1 and the calcium ion. However, its release from calcium and formation of a hydrogen bond with a water molecule allowed to bind to calcium led to more of the negative charge of Glu189 to be lent to Mn_1, facilitating its oxidation and substantially lowering the energetic transition to S_3 by 13 kcal/mol (0.56e V).

The 2014 computational work by Retegan and coworkers (Retegan et al. 2014) explores structures of the $S_2Tyr_Z^{\bullet}$ split signal state originating from each of the S_2 isoforms – open and closed cubane, Fig. 4b. They found that the oxidized $S_2^{A}Tyr_Z^{\bullet}$ and $S_2^{B}Tyr_Z^{\bullet}$ states formed prior to proton removal. The absence of valence isomers with Mn(III) oxidized rather than Tyr_Z implied that chemical modification of the OEC is requisite to advance the S_2-S_3 transition. For both structures, Tyr_Z oxidation reoriented the dipole moment of the OEC, nearly coincident with the Mn_4-W_1 bond and Asp61, suggesting that Tyr_Z oxidation triggers deprotonation from W1 to Asp61. Retegan et al. determined the tyrosyl radical g-tensor with the full model as well with unrelaxed subsets of the full model: $Tyr_Z^{\bullet}$-His with W_4 & HOH542, $Tyr_Z^{\bullet}$-His with W_4, and $Tyr_Z^{\bullet}$-His alone. The model with the least electropositive environment about the tyrosyl (just $Tyr_Z^{\bullet}$-His) showed a substantial increase in the g_x value to 2.0072. This suggests that the predicted g_x value is highly dependent upon the presence of hydrogen-bonding interactions in which calcium-bound water molecules are involved. As such, Retegan et al. propose another role of the heterocation, in structuring water environment and optimizing the hydrogen-bonding network around Tyr_Z; the ordering influence of the Ca^{2+} fine-tunes the function of the Tyr_Z residue by regulating its electron transfer properties. Rappaport (Rappaport et al. 2011) similarly claims that Ca/Sr exchange results in a change in the hydrogen-bonding network and lead to differences in entropy change in the $S_3Y_Z^{\bullet} \rightarrow S_0$ transition; the distribution and conformations of the substrate water molecules is critical to the catalytic rate.

A 2015 article (Vogt et al. 2015a) reported a QM/MM-based study exploring the degree of X-ray photoreduction present in the 1.9 Å CaOEC structure by Umena et al.(Umena et al. 2011) and in the 2.1Å SrOEC structure by

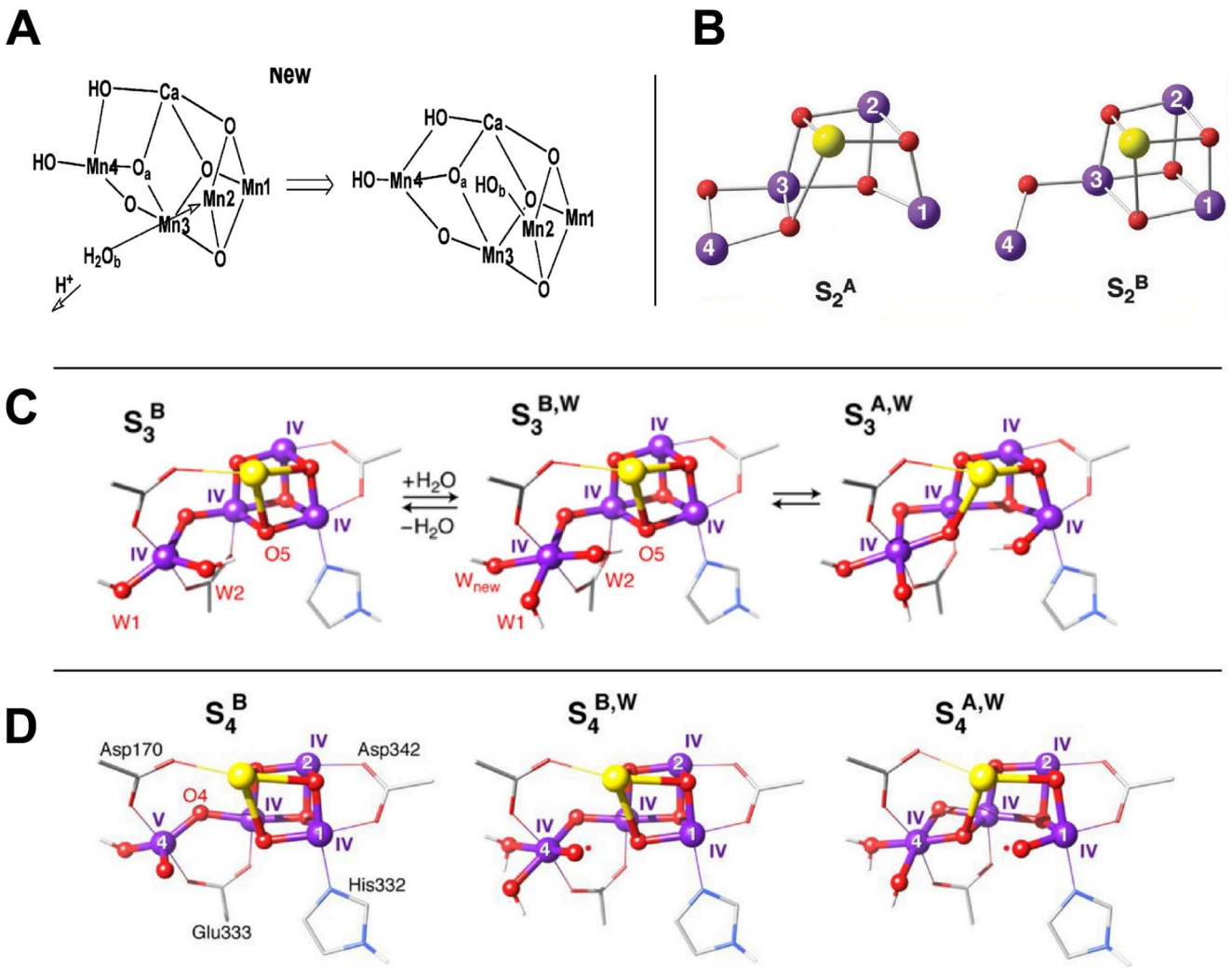

Fig. 4 Different structures relevant to computational modelling of the OEC. **a**) Proposed mechanism for S_2 to S_3 transition, alongside Glu189 forming a hydrogen bond with a Ca-bound water (not shown). Adapted from (Siegbahn 2009). **b**) Structures of the low-spin, open-cubane (S_2^A) and high-spin, closed-cubane (S_2^B) forms introduced in Pantazis et al. (Pantazis et al. 2012). Adapted from (Retegan et al. 2014). **c**) Models of the S_3 and **d**) S_4 states proposed by Krewald et al. Adapted from (Krewald et al. 2019)

Koua et al. (Koua et al. 2013). For both Ca^{2+} and Sr^{2+} OECs, Vogt et al. optimized structures with each cation in the resting dark-stable S_1 state, as well as in a series of sequentially reduced states: S_0, S_{-1}, and S_{-2}. Through comparison to the X-ray crystal structures and the optimized geometries – specifically of the bond lengths from the Ca^{2+}/Sr^{2+} to O_1, O_2, O_5, W_3, and W_2. Their QM/MM models demonstrate that with $Ca^{2+}\rightarrow Sr^{2+}$ substitution, an elongation of the heterocation bonds results, in agreement with XAS results. Based on the structural parameters studied, they suggest that the S_{-2} oxidation state of the Mn_4 complex – corresponding to $Mn_3^{III}Mn^{II}$ – is most consistent with the XRD data for both Ca^{2+} and Sr^{2+}containing PS II. They note that their models only reproduce the O_5 position when the oxygen is protonated; both O_4 and O_5 are coordinated in their models which best fit the XRD data for both heterocations in the S_2 state.

The work of Pitari et al. (Pitari et al. 2015) in 2015 was similarly a QM/MM report inspired by the 2.1 Å XRD structure of the SrOEC; their focus was on modelling Ca^{2+}, Sr^{2+}, and Cd^{2+} models in the S_2 state. They suggested the role of the Ca^{2+} was both structural and functional, citing a difference in the computed pK_a for the water molecule bound to each of the heterocations; for Sr^{2+}, this pK_a value is 0.51 units greater than for Ca^{2+}, and the value for Cd^{2+} was 3.47 units smaller. A report by Amin et al. in 2021 (Amin et al. 2021) presents a DFT-based study with similar findings. Amin et al. employ the B3LYP hybrid functional to study Ca and Sr variants of S_2 and S_3 models; in particular, they examine two S_2 structures: S_{2A}, with a neutral His190, and S_{2B}, where W_3 is deprotonated, resulting in a $His190^+$. They find that the $S_{2A}\rightarrow S_{2B}$ transition is more favorable in the CaOEC than the SrOEC for several choices of double-zeta,

polarized valence basis sets and the B3LYP functional. They also computed the pK_a values of W_3 in the S_2 state; the Sr water's pK_a is 4 units higher – qualitatively similar to previous literature (Pitari et al. 2015). Work by the Guidoni group (Bovi et al. 2013) suggests that the low-spin S_2 state – associated with MLS – is a sequential precursor to the high-spin S_2 state – associated with g = 4.1 signal – towards the formation of S_3, as previously hypothesized (Cox and Messinger 2013).

A 2019 computational work by Krewald and coworkers (Krewald et al. 2019) identifies three spectroscopically distinct structures of the S_3 state and demonstrates that each isomer leads to a structurally distinct S_4 state. Noting the hypothesized isoforms of the S_2 state (open: S = 1/2, S_2^A; closed: S = 5/2, S_2^B) and that the S_2-S_3 transition may proceed with oxidation, deprotonation, and potential coordination of a water molecule, Krewald et al. posit three distinct structural models for the S_3 state: (i) S_3^B, a model of five-coordinate, approximately trigonal-bipyramidal Mn^{IV} coordinated to the $CaMn_3O_4$ cubane; (ii) $S_3^{B,W}$, a closed-cubane model generate by low-barrier water binding at Mn_4 of S_3^B or by direct OH binding at internal site of Mn_4; and (iii) $S_3^{A,W}$, a model with four six-coordinate Mn^{IV}. "W" implies a new water is bound to a manganese ion. See Fig. 4c. The S_3^B state was shown by Retegan et al. (2016) as requisite for S_3 formation, since only the S_2^B component of the S_2 state proceeds to S_3, as demonstrated in prior EPR study. The $S_3^{A,W}$ state is supported by EXAFS simulations and by magnetic resonance studies; (Cox et al. 2014; Askerka et al. 2016) $S_3^{B,W}$ connects the two. Producing S_4 models from these distinct S_3 models was done with consideration of the more studied S_2-S_3 transition; In the S_2 and $S_2Tyr_Z^{\bullet}$ states, the proton removed was part of W1 in the open cubane S_2^A, and W1 is the only Mn-bound H_2O in that state. Applying these considerations lead to the observation that the most acidic protons in $S_3^{A,W}$ and $S_3^{B,W}$ are on newly coordinated waters, the only doubly protonated water ligand; in S_3^B, this proton belongs to either of the hydroxyl ligands W1 or W2. With the observation that following the $S_3Tyr_Z^{\bullet}$ state substrates cannot exchange disfavors deprotonation of a water group in $S_3^{A,W}$ or $S_3^{B,W}$. The resulting 3 models, S_4^B, $S_4^{A,W}$, and $S_4^{B,W}$ were produced (See Fig. 4d). $S_4^{A,W}$ and $S_4^{B,W}$ contain Mn(IV)-oxyl units – $S_4^{A,W}$ is an open-cubane structure with oxyl attached to Mn_1, and $S_4^{B,W}$ is a closed-cubane structure with oxyl *trans* to the W_1 at (octahedral) Mn_4. These contrast to the genuine Mn(V)-oxo produced in the S_4^B model with five-coordinate, trigonal-bipyramidal-like Mn_4. Positioning the unbound water molecule in S_4^B to the second coordination sphere led to the models being energetically indistinguishable relative to the uncertainties of their computational methods. Noting that the high radical character of the oxyl groups in $S_4^{A,W}$ and $S_4^{B,W}$, alongside the increased p/d-mixing of the Mn(V)-oxo group in S_4^B compared to Mn^{IV}-oxyl groups, Krewald suggests spectroscopic signatures of each model, were spectroscopic observation of S_4 intermediates become possible. Spin density on the oxyl radical could be detectable by EPR methods such as O^{17} ENDOR, while Mn K_α pre-edge intensity might reveal the S_4^B intermediate.

Allgöwer et al. (2022) performed a computational study to explore the redox-coupled protonation dynamics in various S-state transitions in photosystem II. They observed that with oxidation of Tyr_Z, conformational changes in the Asp61/Lys317 ion-pair lower the reaction barrier for water mediated proton transfer from W3 (Ca^{2+}-bound) to Asp61. The deprotonation of W_3 substrate water results in its translation towards Mn1, in good agreement with the position identified in recent XFEL-based structures (Ibrahim et al. 2020). Optimized minimum energy reaction pathways reveal that the proton transfer from the Ca^{2+}-bound W3 to Asp61 occurs across a series of five water molecules; the overall reaction barrier was shown to be 14 kcal mol^{-1}. With subsequent oxidation of the OEC, the proton transfer barrier about the water ligand sphere of the OEC is further lowered. Allgöwer et al. ultimately propose a radical-coupling mechanism towards O-O bond formation.

Synthetic analogues

An electrochemistry-based approach by Agapie and Tsui (Tsui and Agapie 2013) investigated compounds of MMn_3O_4 structure (where M →Ca^{2+}, Sr^{2+}, Zn^{2+}, Sc^{3+}, Y^{3+}, and Mn^{3+}). They observed that cluster reduction potentials of these compounds and of similar mixed-metal Mn-tetraoxido complexes correlate with the Lewis acidity of the apical redox-inactive metal. This relates to similar findings for heterometallic Mn-dioxo clusters they worked with prior. The further finding that Ca/Sr-Mn_3O_4 clusters shared similar reduction potentials, combined with the knowledge that Ca and Sr are the only atoms for a functional MMn_4O_5 OEC reinforced the idea that these heterocations may have a role in modulating the reduction potential of the cluster. The relationship in findings between the tetraoxo and dioxo models suggests that the role of the Lewis acidities of the incorporated cations is held across a broadly diverse set of structural motifs. A subsequent computationally focused work by Krewald and coworkers (Krewald et al. 2016) further investigated these findings. They computed the relative redox potentials of various substituted derivatives of the OEC with cations Sr^{2+}, Gd^{3+}, Cd^{2+}, Zn^{2+}, Mg^{2+}, Sc^{3+}, Na^+ and Y^{3+}, across two sequential transitions of the catalytic cycle. This computational approach was first validated against several Mn_3AO_4 model complexes – good structural mimics of the OEC – and found good reproduction of the

empirically observed relationship between Lewis acidities of the cations and reduction potentials of the clusters. However, the correlation was not observed with the OEC substitutions. The cluster's redox potential within the enzyme was dependent upon the charge of the redox-inactive cations; in other words, the redox potential was shown to be insensitive to the identity of the substation, hindering the stance that one primary role of the heterocation is in redox-tuning.

Computational study of synthetic OEC analogues is also worth consideration. The work of Kanady and coworkers (Kanady et al. 2014) presents a synthetic strategy and roadmap for producing accurate synthetic models of the tetramanganese oxygen evolving complex. They synthesized $Mn^{IV}{}_3GdO_4$ and $Mn^{IV}{}_3CaO_4$ cubanes. A procedure of sequential ligand substitutions produced substantial distortions resulting in a highly asymmetric cubane; these models, when coordinated by a fifth metal ion, were able to mirror the structure of the OEC by displaying the known cubane motif alongside a dangling transition metal. Other works led by Zhang (Li et al. 2020; Yao et al. 2021) report synthetic Mn_4XO_4 clusters – X = Ca, Y, Gd – which closely resemble the OEC, closely mirroring the oxidation states of the manganese atoms and overall redox activity. Their works demonstrate the capabilities of rare-Earth metals to structurally replace Ca in neutral Mn_4XO_4 clusters; this challenges the view of the role of Lewis acidity modulating the redox potential of heteronuclear-oxide clusters. These synthetic model compounds improve the capabilities to study electronic structure, spectroscopy and reactivity of the OEC. Of similar interest is the study of the closest-known catalyst analog for PS II: $[Co_4O_4Py_4Ac_4]$ (Py = pyridine and Ac = CH_3COO^-), recently reported upon by several groups (Nguyen et al. 2015; Smith et al. 2015; Ezhov et al. 2021).

Simulated EXAFS analysis of S_3 state models

Here, we examine three computational models, each analogous to those in the preceding computational section, Fig. 5a. We refer to these three S_3 state models as $S_{3\ Mn=O}$: model based on Suga et al. (2017) coordinates (PDB, 5WS6); $S_{3\ Mn-OH}$: a model with a different protonation pattern, with one proton moved from the Mn_4 water to the Mn_1 = O oxo-group forming a Mn_{1D}-OH moiety, and $S_{3\ OO}$: a peroxo isoform of the S_3 state which was hypothesized to be forming prior to the final electron transfer to Tyr_Z. Previous work (Boussac et al. 2015) showed that the capacity of the OEC in S_3 to absorb near-infrared (NIR) light to induce new EPR signals from the OEC S_3 state at cryogenic temperatures suggests the possibility for a potential high-energy intermediate of the S_3 state; other work by our group have demonstrated that such an intermediate may be accessible (+0.2 eV, easily achievable by NIR light, ~1.5 eV), while S_4 generation prior to O-O bond formation does not improve energetics towards O-O bond formation (Pushkar et al. 2018).

Table 2 summarizes the key supporting energies for the driving force and the energies of the S-state transitions; see Tables S3 and S4 for charge, spin, and electronic energies of each model. Note that with computation of redox processes – S-state transitions – we consider both the energies of the proton and electron upon their removal, avoiding the need to compute individual proton energies; as such, we can directly compare computed energies with the energy of the driving force, $Tyr_Z^{\bullet}$ reduction with the PCET process: Tyr-OH = Tyr-O$^{\bullet}$ + e^- + H^+, ~17.55 eV. We have to note that S_3 to S_0 transition, unlike other S-states transitions in Table 2 draws energy greater than available 17.55 eV from $Tyr_Z^{\bullet}$ reduction. This can be due to the imperfection of the DFT model (note QM/MM might be used in the future to allow additional restrains on amino acids positions) or in the sophisticated scheme realized by PS II ligand environment where excess energy in prior S_1-S_3 transitions is stored in conformational or H^+ uphill configurations of higher energy and later released to help the energy demanding S_3 to S_0 transition.

We observe that with the CaOEC Suga model (PDB, 5WS6) as a starting point and substitution of Ca^{2+}→Sr^{2+} followed by DFT optimization – see >Table S2 for a summary of the S_1 geometric differences between the CaOEC and SrOEC models – that a suitably analogous SrOEC S_3 state may be found. In fact, the S_2→S_3 transition is slightly easier for SrOEC than for the CaOEC model. This energy difference $\Delta\Delta E_{Ca\rightarrow Sr}$ is like that of the initial S_1→S_2 transition, with $\Delta\Delta E_{Ca\rightarrow Sr}$ ~0.2 eV. This suggests that when optimized with the BP86 functional, incorporation of water in the S_2→S_3 state transition, alongside the resulting conformational change about the ligating structure to the OEC, the SrOEC S_3 state may be more stabilized relative to CaOEC. Despite the difference in S_3 state energetics, the relative energies of the peroxo S_{3OO} state and the S_3 state between models does not change drastically (0.89 eV for Ca and 1.08 eV for Sr, BP86 functional); the work of Yamaguchi addresses peroxo and superoxo formation models in depth (Isobe et al. 2016, 2019; Yamaguchi et al. 2022).

The prior DFT work on the S_{3OO} state revealed that the B3LYP* functional (containing 15% Hartree-Fock exchange) resulted in a decrease in the energy difference of the peroxo state for CaOEC, a finding that is consistent with other works, notably of Isobe et al. (Isobe et al. 2016).

We do note that the geometric optimization of the SrOEC S_{3OO} state was 0.1 eV more stable in the triplet (S = 1) than quintet (S = 2) spin state. Indeed, when studied previously (Pushkar et al. 2018), the CaOEC peroxo isoform tended to converge to the S_3 state when the system spin exceeded

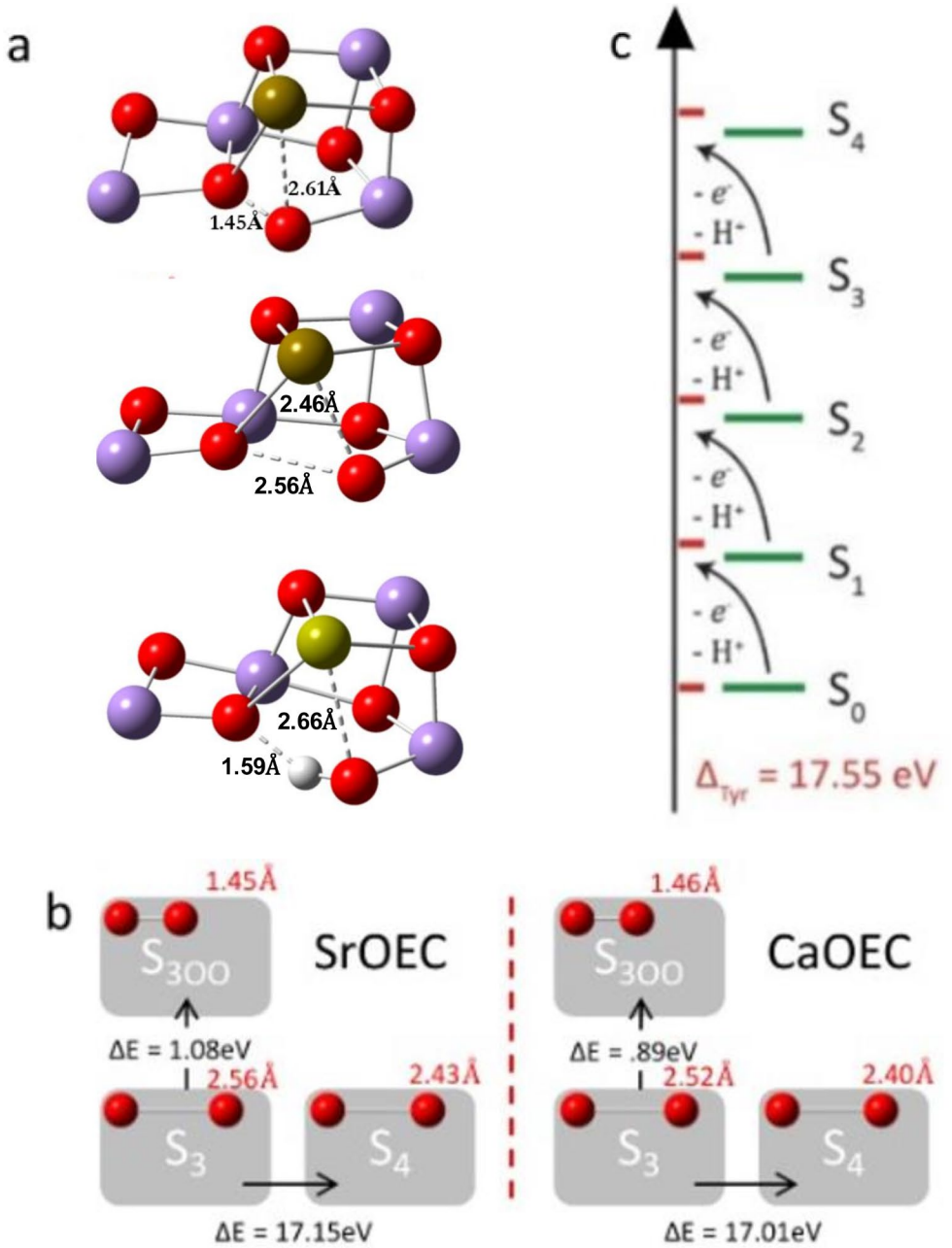

Fig. 5 Schematic summarizing key geometric and energetic results from our DFT study. **a**) Structures of the Sr-substituted S_{3OO} (top), $S_{3Mn=O}$ (middle), and S_{3Mn-OH} (bottom) models. Bond distances of Sr-O_6 and O_5-O_6 are indicated. **b**) Scheme comparing the energies of the S_3, S_{3OO}, and S_4 states for both CaOEC and SrOEC model, using the BP86 functional. **c**) Energy diagram of the S-state transitions with every step been modeled as a proton coupled electron transfer (PCET) to ensure a straight forward comparison with a driving force of Tyr_Z redox couple. Red ticks represent the energy change due to $Tyr_Z^{\bullet}$ reduction with the PCET process: Tyr-OH = Tyr-O$^{\bullet}$ + e^- + H^+. Implicit treatment of protons. Adapted from (Pushkar et al. 2018)

S = 1, though could converge to the peroxo isoform (O_5-O_6 bond distance ~ 1.5 Å) when optimized in the triplet state, a bond distance in good agreement with the 2017 structure of Suga et al. (1.5 Å) but disagreement with their later structure (2.0 Å). SrOEC in the S_3-state converges to a peroxo isoform for both S = 1 (1.45 Å) and S = 2 (1.44 Å). Heisenberg exchange Hamiltonian fitted to broken symmetry calculations was used to confirm the total spin of CaOEC DFT models for the S_3 state (Pushkar et al. 2018). Such analysis for SrOEC is outside the scope of this manuscript, thus listed spin states of the SrOEC DFT models are suggestive at the moment. The $S_3 \rightarrow S_4$ and $S_3 \rightarrow S_0$ transitions proceed with a similar $\Delta\Delta E_{Ca \rightarrow Sr}$ of ~ 0.1 eV and ~ 0.2 eV. Figure 5 summarizes the key geometric and energetic findings of the S_3 and later stages of the Kok cycle for the computed CaOEC and SrOEC models. A refinement of these SrOEC models may be possible with the use of computational methods employing some Hartree-Fock exchange, potentially resulting a further stabilization of the S_{3OO} state for SrOEC. However, the current model predicts a more uphill transition for $S_3 \rightarrow S_{3OO}$ ($\Delta\Delta E_{Ca \rightarrow Sr}$ ~0.2 eV) in SrOEC than in CaOEC, suggesting that access to O-O bond formation early in the S_3-to-S_0 transition is faster for native than SrOEC,

Table 2 Supporting energies for driving force and energies of the S-state transitions*. BP86 methodology, def2tzvp basis set DFT calculations. By considering the energies of both the proton and electron upon their removal, ΔE incorporates their combined contributions, circumventing the need to estimate individual proton energies, which could be subject to significant error

	BP86 / def2tzvp Energy (eV)	
H_2O	-2080.665	
OH^-	-2062.975	
O_2	-4092.570	
Tyr-OH	-8369.840	
Tyr-O$^\bullet$	-8352.286	
Tyr-OH = Tyr-O$^\bullet$ + e^- + H^+	17.55	
	Ca OEC Model (eV)	**Sr OEC Model (eV)**
$S_1 = S_2 + H^+ + e^-$	16.33	16.15
$S_2 + H_2O = S_3 + H^+ + e^-$	17.10	16.88
$S_3 = S_4 + H^+ + e^-$	17.01	17.15
$S_3 + H_2O = S_0 + H^+ + e^- + O_2$	19.45	19.66
$S_3 \rightarrow S_{3OO}$	0.89	1.08

* While release of protons to the lumen is S-state dependent, the Kok cycle was DFT modeled for OEC core with every step been a proton coupled electron transfer (PCET) to ensure a straightforward comparison with a driving force of Tyr_Z redox couple

consistent with the lower rater of oxygen-evolving activity in SrOEC.

With three optimized models for CaOEC, we compute simulated Mn EXAFS – see Methods, supplementary information – for each of the models and compare against experimental data for S_3 state Fig. 6. MnXAS from CaOEC spinach samples was reported earlier (Pushkar et al. 2007) measured by the same techniques as in (Yano et al. 2005b). Each simulated spectrum from each computational model had its amplitude rescaled by a unique multiplicative constant to best fit the experimental data by least squares; see methods in supplementary information. By comparison of least-squares fitting for each computational model's simulated spectrum against the experimental spectrum, the hydroxide model, $S_{3\ Mn-OH}$ provides the best fit. Models of both Mn = O and Mn-OH protonation states on Mn_1 fit the experimental spectrum relatively well until wavenumber 8.5 $Å^{-1}$, at which point all the models fit relatively poorly. Smoothing of the experimental spectrum (Savitzky-Golay algorithm, 10 points) does not substantially change the required vertical scaling of the simulated spectra nor the relative quality of fits and agreement with experiment, Fig. 6, S1-S2, and Table S5. The Fourier transforms of each of the computational models are overlaid against the Fourier transform in the experimental data in Figure S3. The aforementioned peaks I, II, and III are reproduced well for each of the three models, though the relative peak intensities differ slightly. This is easily explained by the selection of k-range used for the Fourier transform; a small difference in range can produce substantial changes in the R-space representation.

Similarly, the XRD structures from Suga et al. in 2017 and 2019 were evaluated and compared with experiment. The more recent 2019 structure provided a better fit than the 2017 structure, Figure S4 and Table S5. The S_{3OO} model and the Suga 2017 XRD structure both feature a very short O_5-O_6 bond distances ~ 1.5 Å. That these provide poor fits with the deconvoluted S_3 state data suggests that such a characteristic is not representative of the S_3-state geometry. Despite both XRD-structure-based models fitting more poorly than DFT-optimized hydroxide models, the XRD-based structures did provide some insights. Despite the maximum scattering distance parameter being set equal in both DFT-optimized

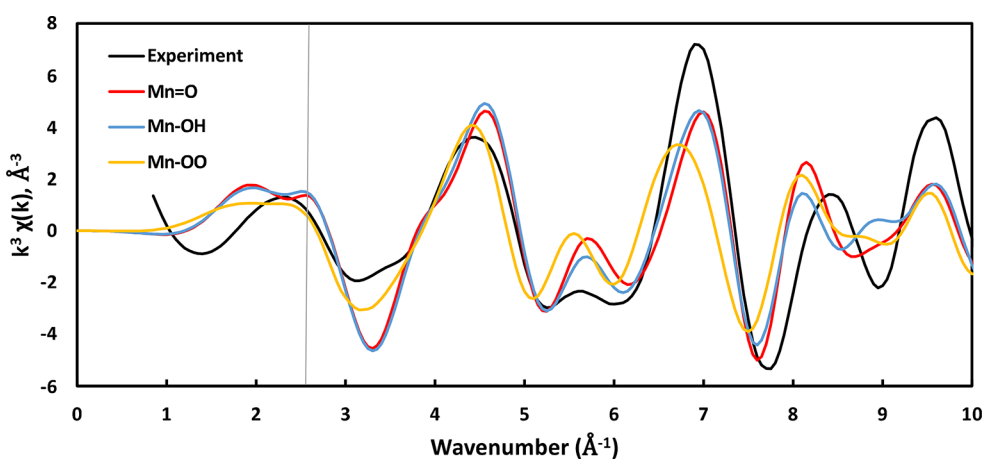

Fig. 6 Overlays of CaOEC Mn EXAFS spectra from spinach and the three computational models discussed. $S_{3\ Mn=O}$: model based on Suga et al. (Suga et al. 2017) coordinates (PDB, 5WS6); $S_{3\ Mn-OH}$: a model with a different protonation pattern, with one proton moved from the Mn_4 water to the Mn_1 = O oxo-group forming a Mn_{1D}-OH moiety, and $S_{3\ OO}$: a peroxo isoform of the S_3 state forming prior to the final electron transfer from Tyr_Z. Fitting is done in the region of 2.6 $Å^{-1}$-10.0 $Å^{-1}$, marked by the vertical gray line. k-weight = 3

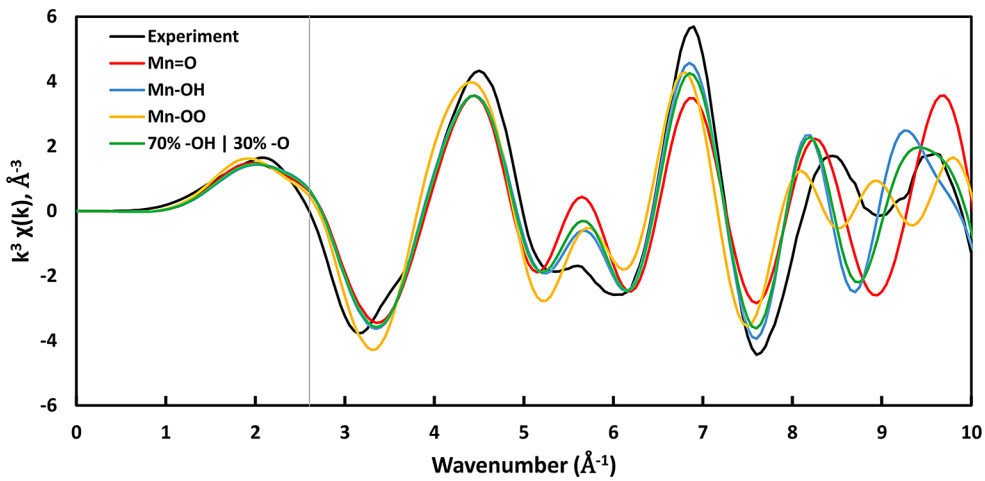

Fig. 7 Overlays of SrOEC Mn EXAFS spectra from experiment and the computational models. Experimental data is smoothed, deconvoluted, twice-flashed *T. elongatus* (Pushkar et al. 2008). $S_{3\ Mn=O}$: model based on Suga et al. (Suga et al. 2017) coordinates (PDB, 5WS6); $S_{3\ Mn-OH}$: a model with a different protonation pattern, with one proton moved from the Mn_4 water to the $Mn_1=O$ oxo-group forming a Mn_{1D}-OH moiety; a linear combination of these, 70% hydroxide model plus 30% Mn = O model; and S_{3OO}: a peroxo isoform of the S_3 state forming prior to the final electron transfer from Tyr_Z. Fitting is done in the region of 2.6 $Å^{-1}$-10.0 $Å^{-1}$, marked by the vertical gray line. k-weight = 3

and XRD-derived structures' simulations and the much larger "model" size of the XRD structures, both approaches yielded the same number of scattering paths per Mn atom. This suggests that DFT model size (~ 110 atoms, containing the tetramanganese cluster and the first ligation sphere) is not a limiting factor in the number of scattering paths and may yield better fits against experimental EXAFS than XRD-based structures.

In a similar way, we will now consider analogous SrOEC models fitted against deconvoluted S_3 state *T. elongatus* experimental Mn EXAFS (Pushkar et al. 2008). The DFT structures were optimized following $Ca^{2+} \rightarrow Sr^{2+}$ substitution in the models of S_1-S_3 states; see methods in supplementary information. With some of the already discussed works highlighting possible heterogeneities of the S_3 state, we will also consider linear combination of the $Mn_{1D}=O$ and Mn_{1D}-OH protonation state models. Figure 7 provides overlays of each of the computational models presented. The combination of x% hydroxide and (100-x)% Mn = O protonation state models was itself optimized by similar least-squares methodology and resulted in 70% Mn-OH and 30% Mn = O model. The improved fit with a linear combination of chemically distinct structures is consistent with recent claims of heterogeneity in the S_3 state. While all three base computational models fit reasonably well at low wavenumber, the linear combination of the Mn-OH and Mn = O models produce a noticeably better fit at high wavenumber, though the ~ 8.5 $Å^{-1}$ wavenumber region provides a poor fit for all simulated spectra. Of the three computational models, the hydroxide-based model provided the best least-squares fit against the experimental data up to k = 10 $Å^{-1}$, and the linear combination model provided a substantially improved fit, Table S5. That a linear combination mostly constituted of the Mn-OH protonation model improves fitting to the experimental spectrum seems appropriate; the simulated Mn and FTs based on the Mn-OH model reproduce experimentally observed (Pushkar et al. 2008) changes in the $S_2 \rightarrow S_3$ transition: a vanishing of peak III, Fig. 5a.

The merits of the linear combination of models EXAFS approach are more pronounced with Sr EXAFS, Fig. 8, S5-6. One immediate observation is that the individual DFT-based models demonstrate a very poor fit against the experimental Sr EXAFS above the ~ 8 $Å^{-1}$. This limited the range of k-space least-squares fitting to a maximum of 7.25 $Å^{-1}$. In this range, the hydroxide model again fits better than the other two computational models, Table S5. However, by repeating the same linear combination of spectra – 70% hydroxide model and 30% Mn = O model – we find a reasonable agreement with experiment, up to wavenumber 10 $Å^{-1}$. Experimental Sr EXAFS has shown that in the $S_2 \rightarrow S_3$ transition, the Mn-Sr peak (~ apparent distance ~ 2 Å) split into two distinct peaks with slightly lower and higher apparent distances (Pushkar et al. 2008). In the simulated spectra, a similar splitting is present for the $S3_{OO}$ and the $S3_{Mn-OH}$ models, less so the $S3_{Mn=O}$ structure, Figure S5b. As is shown in Fig. 7, a linear combination (mostly constituted of the Mn-OH protonation model) of Mn-OH and Mn = O spectra find good agreement with experimental k-space spectra. The fact that the linear combination of Mn-OH (which reproduces experimentally observed FT trends) and Mn = O (which reproduces these Sr FT trends more poorly) models improves the quality of the fit is likely due to a combination of two effects. One is that the linear combination of chemically distinct models may better represent a heterogeneity

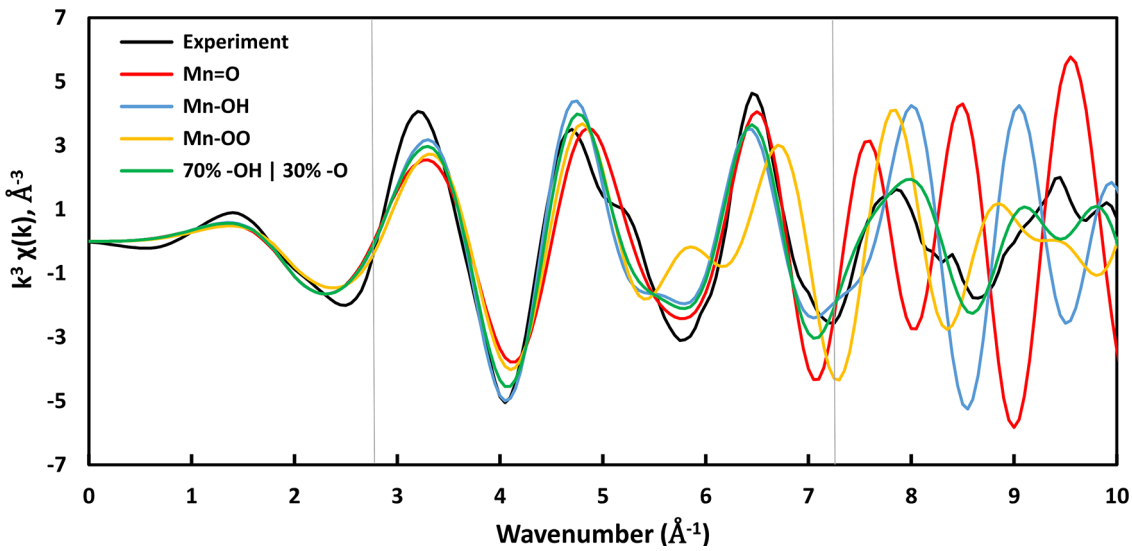

Fig. 8 Overlays of SrOEC Sr EXAFS spectra from experiment (twice-flashed *T. elongatus*, deconvoluted S_3) and the computational models. Experimental data is smoothed, deconvoluted, twice-flashed *T. elongatus* (Pushkar et al. 2008). $S_{3\ Mn=O}$: model based on Suga et al. (Suga et al. 2017) coordinates (PDB, 5WS6); $S_{3\ Mn-OH}$: a model with a different protonation pattern, with one proton moved from the Mn_4 water to the $Mn_1=O$ oxo-group forming a Mn_{1D}-OH moiety; a linear combination of these, 70% hydroxide model plus 30% Mn = O model; and $S_{3\ OO}$: a peroxo isoform of the S_3 state forming prior to the final electron transfer from Tyr_Z. Fitting is done in the region of 2.8 $Å^{-1}$-7.5 $Å^{-1}$, marked by the vertical gray lines. k-weight = 3

in the S_3 state. Additionally, however, there may be effect that a linear combination of different models' Sr EXAFS may capture some of the large degree of structural disorder about Sr: the likely heterogeneity in Sr position and scattering distances; see large Debye-Waller factors for Sr EXAFS fits (Pushkar et al. 2008). Indeed, even simulated Sr EXAFS from the large Koua model (Koua et al. 2013) is unable to capture the decreased amplitude at large wavenumber when compared to an experimental S_2 state spectrum, Figure S6.

Holistically, we can draw several useful conclusions from enumerated comparisons. Computational models of the CaOEC in the S_3 state with a Mn_{1D-OH} moiety provide the best fits against S_3-state experimental data. DFT geometry optimizations on $Ca^{2+} \rightarrow Sr^{2+}$ models demonstrate the same results for SrOEC fitting to experimental EXAFS. Given the similarity of CaOEC and SrOEC Mn EXAFS, that Mn_{1D-OH} remains the best-fitting model to the experimental data is unsurprising and supports the use of the computational model for SrOEC. A similar conclusion was recently achieved via DFT based analysis of high energy resolution fluorescence detected (HERFD) X-ray absorption spectra of the S_3 state showing preference for the model with Mn_{1D-OH} moiety (Chrysina et al. 2023). Turning to Sr EXAFS fitting (Ca EXAFS are non-viable due to difficulties in experimentation at low Ca K-edge energy ~ 4 keV), we find that Sr EXAFS find poor agreement with all experimental models past 7.5 $Å^{-1}$. This suggests possible heterogeneity in Sr position and scattering distances, resulting in greater disagreement with experimental data at higher wavenumber. Given that XRD structures with the same R_{Max} parameter produced the same number of scattering paths as did the CaOEC DFT models, this aspect is likely not responsible for the poor agreement at high wavenumber. DFT-based models that extend beyond the second ligation sphere about the OEC, or models with appropriate structural constraints upon the first ligation sphere may better model the protein environment about the OEC. This is especially true for SrOEC, which are modelled as a perturbation of the CaOEC models derived from XRD structure. "SrOEC 2F" XRD structures may inform models able to be better fit to Sr EXAFS and gain insight into the heterocation EXAFS. However, if we consider proposals of a heterogeneity in the S_3 state and apply them to the current least-squares fitting methodology applied to DFT-optimized models, we can find stronger agreement with experiment, particularly for the Sr EXAFS simulations. Given that a linear combination of different S_3 models – or a heterogenous S_3 state model – with different protonation on Mn_{1D} were able to fit experiment in ways single structure modelling cannot, we cannot exclude the possibility of a heterogeneity in the S_3 state. Furthermore, such a modelling approach may address the likely heterogeneity of Sr position and scattering distances in Sr-substituted specimens.

Conclusions

The study of natural photosynthesis informs the study of artificial photosynthesis and inspires rational design of water oxidation catalysts. With this investigation into the effects of Ca^{2+}→Sr^{2+} substitution in the OEC of PS II, we can hope to achieve mechanistic insights transferable to designs of artificial systems. Early hypotheses suggested that the role of the heterocation in the OEC was in altering the redox chemistry of the cluster itself; indeed, many cubane-like model compounds demonstrated altered redox chemistry with different alkaline and atomic substitutions. However, in the more complex OEC, similar findings were not observed. Further computational and electrochemical study then investigated the influence of Ca^{2+} and Sr^{2+} on water pathways and hydrogen-bonding networks. Indeed, the Ca^{2+}/Sr^{2+} ion is coordinated by two waters and forms a hydrogen-bonded network ending at the redox-active Tyr_Z. Many works have suggested the subtle 0.1–0.2 Å increase in Mn-Mn and Mn-Sr bond distances resulting from Ca^{2+}→Sr^{2+} substitution, and this could very possibly disturb the hydrogen-bonding network and alter the electrochemistry of the redox active moiety; such has been suggested by both computational and EPR study. This influence on a redox-active unit then finds agreement with electrochemical studies on model cubane systems. Similar computational works explored the movement of substrate waters about the calcium atom; conformational changes about the tetramanganese cluster may then disrupt the hydrogen bonding network facilitating the substrate waters' movement. Given these insights, it is possible that the Ca^{2+}→Sr^{2+} substitution is the only one which maintains sufficiently similar valence chemistry while perturbing the surrounding water and hydrogen-bonding network minimally to retain oxygen-evolving activity.

To reveal insights into the O-O bond formation chemistry of PS II, researchers have employed a variety of experimental and computational techniques, directed both at the protein and through model complexes. One means with which to probe the OEC core of the photosynthetic protein is the replacement of Ca^{2+} with Sr^{2+}, the only atom substitution able to retain (diminished) oxygen-evolving activity. These investigations encompassed native cyanobacteria and spinach variants with Ca-based systems, as well as proteins grown and reconstituted with Sr. The development of ever-higher resolution crystal structures of the OEC prepared in various stages of the Kok cycle, as well as the emergence of sophisticated DFT and QM/MM models consistent with the spectroscopic data, yield substantial insights into the mechanistic and structural effects of Ca^{2+}→Sr^{2+} substitution. These combined studies overall do not contradict the hypothesis of O-O bond formation through O_5 and O_6. Such an interaction could occur with a peroxo-like formation in the $S_3Tyr_Z^{\cdot}$ oxidation state, prior to the final oxidation event. These collective efforts aim to develop a robust mechanistic understanding of the O-O bond formation process in PS II, Nature's finest catalyst. Moreover, these developments contribute substantially to the ongoing pursuit of designing artificial water-splitting catalysts capable of addressing the world's current energy crisis through sustainable means.

Supplementary Information The online version contains supplementary material available at https://doi.org/10.1007/s11120-024-01117-2.

Acknowledgements This research was supported by the NSF, CHE-2303743 (Y.P.) and by GM132024 (T32 Molecular Biophysics Training Program to G.B.) from the National Institute of General Medicinal Sciences (NIGMS). We thank Dr Alireza K. Ravari for the helpful discussion.

Author contributions G.B.: writing – original draft preparation; data curation; investigation; methodology. Y.P.: writing – review and editing; supervision, project administration; funding acquisition; conceptualization. All authors have read and agreed to the published version of the manuscript.

Data availability No datasets were generated or analysed during the current study.

Declarations

Competing interests The authors declare no competing interests.

References

Allgöwer F, Gamiz-Hernandez AP, Rutherford AW, Kaila VRI (2022) Molecular principles of redox-coupled protonation dynamics in photosystem II. J Am Chem Soc 144:7171–7180

Amin M, Kaur D, Gunner MR, Brudvig G (2021) Toward understanding the S2-S3 transition in the Kok cycle of Photosystem II: lessons from Sr-substituted structure. Inorg Chem Commun 133:108890

Askerka M, Wang J, Vinyard DJ, Brudvig GW, Batista VS (2016) S3 state of the O2-evolving complex of photosystem II: insights from QM/MM, EXAFS, and femtosecond X-ray diffraction. Biochemistry 55:981–984

Baumgarten M, Philo JS, Dismukes GC (1990) Mechanism of photoinhibition of photosynthetic water oxidation by chloride depletion and fluoride substitution: oxidation of a protein residue. Biochemistry 29:10814–10822

Beal NJ, Corry TA, O'Malley PJ (2018) A comparison of experimental and broken symmetry density functional theory (BS-DFT) calculated electron paramagnetic resonance (EPR) parameters for intermediates involved in the S2 to S3 state transition of nature's oxygen evolving complex. J Phys Chem B 122:1394–1407

Bhowmick A, Hussein R, Bogacz I, Simon PS, Ibrahim M, Chatterjee R, Doyle MD, Cheah MH, Fransson T, Chernev P (2023) Structural evidence for intermediates during O2 formation in photosystem II. Nature 1–8

Biesiadka J, Loll B, Kern J, Irrgang K-D, Zouni A (2004) Crystal structure of cyanobacterial photosystem II at 3.2 Å resolution: a closer look at the Mn-cluster. Phys Chem Chem Phys 6:4733–4736

Boussac A, Rutherford AW (1988) Nature of the inhibition of the oxygen-evolving enzyme of photosystem II induced by sodium chloride washing and reversed by the addition of calcium (2+) or strontium (2+). Biochemistry 27:3476–3483

Boussac A, Rutherford AW (1995) Does the formation of the S3-state in Ca2+-depleted Photosystem II correspond to an oxidation of tyrosine Z detectable by cw-EPR at room temperature? Biochim. Biophys Acta (BBA)-Bioenergetics 1230:195–201

Boussac A, Rutherford AW (2000) Comparative study of the g = 4.1 EPR signals in the S2 state of photosystem II. Biochim Biophys Acta (BBA)-Bioenergetics 1457:145–156

Boussac A, Zimmermann JL, Rutherford AW (1989) EPR signals from modified charge accumulation states of the oxygen-evolving enzyme in calcium-deficient photosystem II. Biochemistry 28:8984–8989

Boussac A, Zimmermann J-L, Rutherford AW (1990) Factors influencing the formation of modified S2 EPR signal and the S3 EPR signal in Ca2+-depleted photosystem II. FEBS Lett 277:69–74

Boussac A, Setif P, Rutherford AW (1992) Inhibition of tyrosine Z photooxidation after formation of the S3-state in calcium-depleted and chloride-depleted photosystem-II. Biochemistry 31:1224–1234

Boussac A, Girerd J-J, Rutherford AW (1996) Conversion of the spin state of the manganese complex in photosystem II induced by near-infrared light. Biochemistry 35:6984–6989

Boussac A, Un S, Horner O, Rutherford AW (1998) High-spin states (S ≥ 5/2) of the Photosystem II manganese complex. Biochemistry 37:4001–4007

Boussac A, Sugiura M, Inoue Y, Rutherford AW (2000) EPR study of the oxygen evolving complex in his-tagged photosystem II from the cyanobacterium Synechococcus elongatus. Biochemistry 39:13788–13799

Boussac A, Rappaport F, Carrier P, Verbavatz J-M, Gobin R, Kirilovsky D, Rutherford AW, Sugiura M (2004) Biosynthetic Ca2+/Sr2 + exchange in the photosystem II oxygen-evolving enzyme of Thermosynechococcus Elongatus. J Biol Chem 279:22809–22819

Boussac A, Sugiura M, Lai T-L, Rutherford AW (2008) Low-temperature photochemistry in photosystem II from Thermosynechococcus elongatus induced by visible and near-infrared light. Philos Trans R Soc B Biol Sci 363:1203–1210

Boussac A, Sugiura M, Rutherford AW, Dorlet P (2009) Complete EPR spectrum of the S3-State of the Oxygen-Evolving Photosystem II. J Am Chem Soc 131:5050–5051

Boussac A, Rutherford AW, Sugiura M (2015) Electron transfer pathways from the S2-states to the S3-states either after a Ca2+/Sr2 + or a Cl–/I– exchange in Photosystem II from Thermosynechococcus Elongatus. Biochim Biophys Acta (BBA)-Bioenergetics 1847:576–586

Boussac A, Ugur I, Marion A, Sugiura M, Kaila VRI, Rutherford AW (2018) The low spin-high spin equilibrium in the S2-state of the water oxidizing enzyme. Biochim Biophys Acta (BBA)-Bioenergetics 1859:342–356

Bovi D, Narzi D, Guidoni L (2013) The S2 state of the oxygen-evolving complex of photosystem II explored by QM/MM dynamics: spin surfaces and metastable states suggest a reaction path towards the S3 state. Angew Chemie 125:11960–11965

Chrysina M, Drosou M, Castillo RG, Reus M, Neese F, Krewald V, Pantazis DA, DeBeer S (2023) Nature of S-states in the oxygen-evolving complex resolved by high-energy resolution fluorescence detected X-ray absorption spectroscopy. J Am Chem Soc 145:25579–25594

Chu H-A, Sackett H, Babcock GT (2000) Identification of a Mn–O–mn cluster vibrational mode of the oxygen-evolving complex in photosystem II by low-frequency FTIR spectroscopy. Biochemistry 39:14371–14376

Chukhutsina VU, Holzwarth AR, Croce R (2019) Time-resolved fluorescence measurements on leaves: principles and recent developments. Photosynth Res 140:355–369

Cinco RM, Robblee JH, Rompel A, Fernandez C, Yachandra VK, Sauer K, Klein MP (1998) Strontium EXAFS reveals the proximity of calcium to the manganese cluster of oxygen-evolving photosystem II. J Phys Chem B 102:8248–8256

Cinco RM, Holman MF, Robblee KL, Yano JH, Pizarro J, Bellacchio SA, Sauer E, K., Yachandra VK (2002) Calcium EXAFS establishes the Mn-Ca cluster in the oxygen-evolving complex of photosystem II. Biochemistry 41:12928–12933

Cinco RM, Robblee JH, Messinger J, Fernandez C, Holman KLM, Sauer K, Yachandra VK (2004) Orientation of calcium in the Mn4Ca cluster of the oxygen-evolving complex determined using polarized strontium EXAFS of photosystem II membranes. Biochemistry 43:13271–13282

Cox N, Messinger J (2013) Reflections on substrate water and dioxygen formation. Biochim Biophys Acta (BBA)-Bioenergetics 1827:1020–1030

Cox N, Rapatskiy L, Su J-H, Pantazis DA, Sugiura M, Kulik L, Dorlet P, Rutherford AW, Neese F, Boussac A (2011) Effect of Ca2+/Sr2 + substitution on the electronic structure of the oxygen-evolving complex of photosystem II: a combined multifrequency EPR, 55Mn-ENDOR, and DFT study of the S2 state. J Am Chem Soc 133:3635–3648

Cox N, Retegan M, Neese F, Pantazis DA, Boussac A, Lubitz W (2014) Electronic structure of the oxygen-evolving complex in photosystem II prior to OO bond formation. Science 345:804–808 (80-.)

Cox N, Pantazis DA, Lubitz W (2020) Current understanding of the mechanism of water oxidation in photosystem II and its relation to XFEL data. Annu Rev Biochem 89:795–820

Dau H, Iuzzolino L, Dittmer J (2001) The tetra-manganese complex of photosystem II during its redox cycle–X-ray absorption results and mechanistic implications. Biochim Biophys Acta (BBA)-Bioenergetics 1503:24–39

Dau H, Liebisch P, Haumann M (2004) The structure of the manganese complex of Photosystem II in its dark-stable S 1-state—EXAFS results in relation to recent crystallographic data. Phys Chem Chem Phys 6:4781–4792

Davis KM, Pushkar YN (2015) Structure of the oxygen evolving complex of photosystem II at room temperature. J Phys Chem B 119:3492–3498

de Lichtenberg C, Rapatskiy L, Reus M, Heyno E, Schnegg A, Nowaczyk MM, Lubitz W, Messinger J, Cox N (2024) Assignment of the slowly exchanging substrate water of nature's water-splitting cofactor. Proc. Natl. Acad. Sci. 121, e2319374121

de Paula JC, Beck WF, Miller A-F, Wilson RB, Brudvig GW (1987) Studies of the manganese site of Photosystem II by electron spin resonance spectroscopy. J Chem Soc Faraday Trans 1 Phys Chem Condens Phases 83:3635–3651

Dekker JP, Ghanotakis DF, Plijter JJ, Van Gorkom HJ, Babcock GT (1984) Kinetics of the oxygen-evolving complex in salt-washed photosystem II preparations. Biochim Biophys Acta (BBA)-Bioenergetics 767:515–523

Ezhov R, Ravari AK, Bury G, Smith PF, Pushkar Y (2021) Do multinuclear 3d metal catalysts achieve O–O bond formation via radical coupling or via water nucleophilic attack? WNA leads the way in [Co4O4] n+. Chem Catal 1:407–422

Ferreira KN, Iverson TM, Maghlaoui K, Barber J, Iwata S (2004) Architecture of the photosynthetic oxygen-evolving center. Science 303:1831–1838 (80-.)

Gates C, Ananyev G, Dismukes GC (2016) The strontium inorganic mutant of the water oxidizing center (CaMn4O5) of PSII improves WOC efficiency but slows electron flux through the terminal acceptors. Biochim Biophys Acta (BBA)-Bioenergetics 1857:1550–1560

Gerey B, Gouré E, Fortage J, Pécaut J, Collomb M-N (2016) Manganese-calcium/strontium heterometallic compounds and their relevance for the oxygen-evolving center of photosystem II. Coord Chem Rev 319:1–24

Ghanotakis DF, Babcock GT, Yocum CF (1984a) Calcium reconstitutes high rates of oxygen evolution in polypeptide depleted photosystem II preparations. FEBS Lett 167:127–130

Ghanotakis DF, Topper JN, Babcock GT, Yocum CF (1984b) Water-soluble 17 and 23 kDa polypeptides restore oxygen evolution activity by creating a high-affinity binding site for Ca2 + on the oxidizing side of Photosystem II. FEBS Lett 170:169–173

Grabolle M, Haumann M, Müller C, Liebisch P, Dau H (2006) Rapid loss of structural motifs in the manganese complex of oxygenic photosynthesis by X-ray irradiation at 10–300 K. J Biol Chem 281:4580–4588

Greife P, Schönborn M, Capone M, Assunção R, Narzi D, Guidoni L, Dau H (2023) The electron–proton bottleneck of photosynthetic oxygen evolution. Nature 617:623–628

Guo Z, Barry BA (2017) Calcium, ammonia, redox-active tyrosine YZ, and proton-coupled electron transfer in the photosynthetic oxygen-evolving complex. J Phys Chem B 121:3987–3996

Guo Z, He J, Barry BA (2018) Calcium, conformational selection, and redox-active tyrosine YZ in the photosynthetic oxygen-evolving cluster. Proc Natl Acad Sci 115:5658–5663

Haddy A, Lakshmi KV, Brudvig GW, Frank HA (2004) Q-band EPR of the S2 state of photosystem II confirms an S = 5/2 origin of the X-band g = 4.1 signal. Biophys J 87:2885–2896

Hasegawa K, Ono T, Inoue Y, Kusunoki M (1999) How to evaluate the structure of a tetranuclear mn cluster from magnetic and EXAFS data: case of the S2-state Mn-cluster in photosystem II. Bull Chem Soc Jpn 72:1013–1023

Haumann M, Müller C, Liebisch P, Iuzzolino L, Dittmer J, Grabolle M, Neisius T, Meyer-Klaucke W, Dau H (2005) Structural and oxidation state changes of the photosystem II manganese complex in four transitions of the water oxidation cycle (S0→ S1, S1→ S2, S2→ S3, and S3, 4→ S0) characterized by X-ray absorption spectroscopy at 20 K and room temperature. Biochemistry 44:1894–1908

Ibrahim M, Fransson T, Chatterjee R, Cheah MH, Hussein R, Lassalle L, Sutherlin KD, Young ID, Fuller FD, Gul S (2020) Untangling the sequence of events during the S2→ S3 transition in photosystem II and implications for the water oxidation mechanism. Proc Natl Acad Sci 117:12624–12635

Ishida N, Sugiura M, Rappaport F, Lai T-L, Rutherford AW, Boussac A (2008) Biosynthetic exchange of bromide for chloride and strontium for calcium in the photosystem II oxygen-evolving enzymes. J Biol Chem 283:13330–13340

Isobe H, Shoji M, Shen J-R, Yamaguchi K (2016) Chemical equilibrium models for the S3 state of the oxygen-evolving complex of photosystem II. Inorg Chem 55:502–511

Isobe H, Shoji M, Suzuki T, Shen J-R, Yamaguchi K (2019) Spin, valence, and structural isomerism in the S3 state of the oxygen-evolving complex of photosystem II as a manifestation of multimetallic cooperativity. J Chem Theory Comput 15:2375–2391

Kamiya N, Shen J-R (2003) Crystal structure of oxygen-evolving photosystem II from Thermosynechococcus Vulcanus at 3.7-Å resolution. Proc Natl Acad Sci 100:98–103

Kanady JS, Lin P-H, Carsch KM, Nielsen RJ, Takase MK, Goddard III, W. A., Agapie T (2014) Toward models for the full oxygen-evolving complex of photosystem II by ligand coordination to lower the symmetry of the Mn3CaO4 cubane: demonstration that electronic effects facilitate binding of a fifth metal. J Am Chem Soc 136:14373–14376

Kern J, Chatterjee R, Young ID, Fuller FD, Lassalle L, Ibrahim M, Gul S, Fransson T, Brewster AS, Alonso-Mori R (2018) Structures of the intermediates of Kok's photosynthetic water oxidation clock. Nature 563:421–425

Kim CJ, Debus RJ (2017) Evidence from FTIR difference spectroscopy that a substrate H2O molecule for O2 formation in photosystem II is provided by the ca ion of the catalytic Mn4CaO5 cluster. Biochemistry 56:2558–2570

Kim SH, Gregor W, Peloquin JM, Brynda M, Britt RD (2004) Investigation of the calcium-binding site of the oxygen evolving complex of photosystem II using 87Sr ESEEM spectroscopy. J Am Chem Soc 126:7228–7237

Klauss A, Haumann M, Dau H (2015) Seven steps of alternating electron and proton transfer in photosystem II water oxidation traced by time-resolved photothermal beam deflection at improved sensitivity. J Phys Chem B 119:2677–2689

Kok B, Forbush B, McGloin M (1970) Cooperation of charges in photosynthetic O2 evolution–I. A linear four step mechanism. Photochem Photobiol 11:457–475

Koua FHM, Umena Y, Kawakami K, Shen J-R (2013) Structure of Sr-substituted photosystem II at 2.1 Å resolution and its implications in the mechanism of water oxidation. Proc. Natl. Acad. Sci. 110, 3889–3894

Krewald V, Neese F, Pantazis DA (2016) Redox potential tuning by redox-inactive cations in nature's water oxidizing catalyst and synthetic analogues. Phys Chem Chem Phys 18:10739–10750

Krewald V, Neese F, Pantazis DA (2019) Implications of structural heterogeneity for the electronic structure of the final oxygen-evolving intermediate in photosystem II. J Inorg Biochem 199:110797

Kulik L, Epel B, Messinger J, Lubitz W (2005a) Pulse EPR, 55 Mn-ENDOR and ELDOR-detected NMR of the S 2-state of the oxygen evolving complex in Photosystem II. Photosynth Res 84:347–353

Kulik LV, Epel B, Lubitz W, Messinger J (2005b) 55Mn pulse ENDOR at 34 GHz of the S0 and S2 states of the oxygen-evolving complex in photosystem II. J Am Chem Soc 127:2392–2393

Li Y, Yao R, Chen Y, Xu B, Chen C, Zhang C (2020) Mimicking the catalytic center for the water-splitting reaction in photosystem II. Catalysts 10:185

Liang W, Roelofs TA, Cinco RM, Rompel A, Latimer MJ, Yu WO, Sauer K, Klein MP, Yachandra VK (2000) Structural change of the Mn Cluster during the S2→S3 state transition of the Oxygen-Evolving Complex of Photosystem II. Does it reflect the onset of Water/Substrate oxidation? Determination by Mn X-ray absorption spectroscopy. J Am Chem Soc 122:3399–3412

Lohmiller T, Krewald V, Navarro MP, Retegan M, Rapatskiy L, Nowaczyk MM, Boussac A, Neese F, Lubitz W, Pantazis DA (2014) Structure, ligands and substrate coordination of the oxygen-evolving complex of photosystem II in the S 2 state: a combined EPR and DFT study. Phys Chem Chem Phys 16:11877–11892

Loll B, Kern J, Saenger W, Zouni A, Biesiadka J (2005) Towards complete cofactor arrangement in the 3.0 Å resolution structure of photosystem II. Nature 438:1040–1044

Lubitz W, Chrysina M, Cox N (2019) Water oxidation in photosystem II. Photosynth Res 142:105–125

Mathe Z, Pantazis DA, Lee HB, Gnewkow R, Van Kuiken BE, Agapie T, DeBeer S (2019) Calcium valence-to-core X-ray emission spectroscopy: a sensitive probe of oxo protonation in structural models of the oxygen-evolving complex. Inorg Chem 58:16292–16301

McEvoy JP, Brudvig GW (2006) Water-splitting chemistry of photosystem II. Chem Rev 106:4455–4483

Messinger J, Robblee JH, Bergmann U, Fernandez C, Glatzel P, Visser H, Cinco RM, McFarlane KL, Bellacchio E, Pizarro SA (2001)

Absence of Mn-centered oxidation in the S2→ S3 transition: implications for the mechanism of photosynthetic water oxidation. J Am Chem Soc 123:7804–7820

Miqyass M, Marosvölgyi MA, Nagel Z, Yocum CF, van Gorkom HJ (2008) S-state dependence of the calcium requirement and binding characteristics in the oxygen-evolving complex of photosystem II. Biochemistry 47:7915–7924

Miyao M, Murata N (1984) Calcium ions can be substituted for the 24-kDa polypeptide in photosynthetic oxygen evolution. FEBS Lett 168:118–120

Miyao M, Murata N (1986) Light-dependent inactivation of photosynthetic oxygen evolution during NaCl treatment of photosystem II particles: the role of the 24-kDa protein. Photosynth Res 10:489–496

Müh F, Zouni A (2020) Structural basis of light-harvesting in the photosystem II core complex. Protein Sci 29:1090–1119

Nguyen AI, Ziegler MS, Oña-Burgos P, Sturzbecher-Hohne M, Kim W, Bellone DE, Tilley TD (2015) Mechanistic investigations of water oxidation by a molecular cobalt oxide analogue: evidence for a highly oxidized intermediate and exclusive terminal oxo participation. J Am Chem Soc 137:12865–12872

Nilsson H, Rappaport F, Boussac A, Messinger J (2014) Substrate–water exchange in photosystem II is arrested before dioxygen formation. Nat Commun 5:4305

Ono T, Inoue Y (1990) Abnormal redox reactions in photosynthetic O2-evolving centers in NaCl/EDTA-washed PS II. A dark-stable EPR multiline signal and an unknown positive charge accumulator. Biochim Biophys Acta (BBA)-Bioenergetics 1020:269–277

Pantazis DA, Orio M, Petrenko T, Zein S, Lubitz W, Messinger J, Neese F (2009) Structure of the oxygen-evolving complex of photosystem II: information on the S 2 state through quantum chemical calculation of its magnetic properties. Phys Chem Chem Phys 11:6788–6798

Pantazis DA, Ames W, Cox N, Lubitz W, Neese F (2012) Two interconvertible structures that explain the spectroscopic properties of the oxygen-evolving complex of photosystem II in the S2 state. Angew Chemie Int Ed 51:9935–9940

Pérez Navarro M, Ames WM, Nilsson H, Lohmiller T, Pantazis DA, Rapatskiy L, Nowaczyk MM, Neese F, Boussac A, Messinger J (2013) Ammonia binding to the oxygen-evolving complex of photosystem II identifies the solvent-exchangeable oxygen bridge (μ-oxo) of the manganese tetramer. Proc Natl Acad Sci 110:15561–15566

Pitari F, Bovi D, Narzi D, Guidoni L (2015) Characterization of the Sr2+-and Cd2+-substituted oxygen-evolving complex of photosystem II by quantum mechanics/molecular mechanics calculations. Biochemistry 54:5959–5968

Poddar H, Heyes DJ, Schirò G, Weik M, Leys D, Scrutton NS (2022) A guide to time-resolved structural analysis of light-activated proteins. FEBS J 289:576–595

Pokhrel R, Brudvig GW (2014) Oxygen-evolving complex of photosystem II: correlating structure with spectroscopy. Phys Chem Chem Phys 16:11812–11821

Pushkar Y, Yano J, Glatzel P, Messinger J, Lewis A, Sauer K, Bergmann U, Yachandra V (2007) Structure and orientation of the Mn4Ca cluster in plant photosystem II membranes studied by polarized range-extended X-ray absorption Spectroscopy*♦. J Biol Chem 282:7198–7208

Pushkar Y, Yano J, Sauer K, Boussac A, Yachandra VK (2008) Structural changes in the Mn4Ca cluster and the mechanism of photosynthetic water splitting. Proc Natl Acad Sci 105:1879–1884

Pushkar Y, Davis KM, Palenik MC (2018) Model of the oxygen evolving complex which is highly predisposed to O–O bond formation. J Phys Chem Lett 9:3525–3531

Pushkar Y, Ravari K, Jensen A, S. C., Palenik M (2019) Early binding of substrate oxygen is responsible for a spectroscopically distinct S2 state in photosystem II. J Phys Chem Lett 10:5284–5291

Rapatskiy L, Cox N, Savitsky A, Ames WM, Sander J, Nowaczyk MM, Rögner M, Boussac A, Neese F, Messinger J (2012) Detection of the water-binding sites of the oxygen-evolving complex of photosystem II using W-band 17O electron–electron double resonance-detected NMR spectroscopy. J Am Chem Soc 134:16619–16634

Rappaport F, Ishida N, Sugiura M, Boussac A (2011) Ca 2 + determines the entropy changes associated with the formation of transition states during water oxidation by photosystem II. Energy Environ Sci 4:2520–2524

Retegan M, Cox N, Lubitz W, Neese F, Pantazis DA (2014) The first tyrosyl radical intermediate formed in the S 2–S 3 transition of photosystem II. Phys Chem Chem Phys 16:11901–11910

Retegan M, Krewald V, Mamedov F, Neese F, Lubitz W, Cox N, Pantazis DA (2016) A five-coordinate mn (IV) intermediate in biological water oxidation: spectroscopic signature and a pivot mechanism for water binding. Chem Sci 7:72–84

Robblee JH, Messinger J, Cinco RM, McFarlane KL, Fernandez C, Pizarro SA, Sauer K, Yachandra VK (2002) The Mn cluster in the S0 state of the oxygen-evolving complex of photosystem II studied by EXAFS spectroscopy: are there three di-μ-oxo-bridged Mn2 moieties in the tetranuclear mn complex? J Am Chem Soc 124:7459–7471

Sanakis Y, Sarrou J, Zahariou G, Petrouleas V (2008) Q-band Electron Paramagnetic Resonance studies of the S3 state of the OEC of Photosystem II BT - Photosynthesis. Energy from the Sun. In: Gantt JF, Golbeck E, J. H., Osmond B (eds) 479–482. Allen. Springer Netherlands, Dordrecht

Service RJ, Hillier W, Debus RJ (2010) Evidence from FTIR Difference Spectroscopy of an Extensive Network of Hydrogen Bonds near the oxygen-evolving Mn4Ca cluster of Photosystem II Involving D1-Glu65, D2-Glu312, and D1-Glu329. Biochemistry 49:6655–6669

Shen J-R, Katoh S (1991) Inactivation and calcium-dependent reactivation of oxygen evolution in photosystem II preparations treated at pH 3.0 or with high concentrations of NaCl. Plant cell Physiol 32:439–446

Shevela D, Kern JF, Govindjee G, Messinger J (2023) Solar energy conversion by photosystem II: principles and structures. Photosynth Res 156:279–307

Siegbahn PEM (2006) O— O bond formation in the S4 state of the oxygen-evolving complex in photosystem II. Chem Eur J 12:9217–9227

Siegbahn PEM (2008) A structure-consistent mechanism for dioxygen formation in photosystem II. Chem Eur J 14:8290–8302

Siegbahn PEM (2009) Structures and energetics for O2 formation in photosystem II. Acc Chem Res 42:1871–1880

Siegbahn PEM, Crabtree RH (1999) Manganese oxyl radical intermediates and O–O bond formation in photosynthetic oxygen evolution and a proposed role for the calcium cofactor in photosystem II. J Am Chem Soc 121:117–127

Simon PS, Makita H, Bogacz I, Fuller F, Bhowmick A, Hussein R, Ibrahim M, Zhang M, Chatterjee R, Cheah MH (2023) Capturing the sequence of events during the water oxidation reaction in photosynthesis using XFELs. FEBS Lett 597:30–37

Sivaraja M, Tso J, Dismukes GC (1989) A calcium-specific site influences the structure and activity of the manganese cluster responsible for photosynthetic water oxidation. Biochemistry 28:9459–9464

Smith PF, Hunt L, Laursen AB, Sagar V, Kaushik S, Calvinho KUD, Marotta G, Mosconi E, De Angelis F, Dismukes GC (2015) Water oxidation by the [Co4O4 (OAc) 4 (py) 4] + cubium is initiated by OH–addition. J Am Chem Soc 137:15460–15468

Sproviero EM, Gascón JA, McEvoy JP, Brudvig GW, Batista VS (2008) A model of the Oxygen-Evolving Center of Photosystem II predicted by structural refinement based on EXAFS simulations. J Am Chem Soc 130:6728–6730

Strickler MA, Walker LM, Hillier W, Debus RJ (2005) Evidence from biosynthetically incorporated strontium and FTIR difference spectroscopy that the C-terminus of the D1 polypeptide of photosystem II does not ligate calcium. Biochemistry 44:8571–8577

Suga M, Akita F, Sugahara M, Kubo M, Nakajima Y, Nakane T, Yamashita K, Umena Y, Nakabayashi M, Yamane T (2017) Light-induced structural changes and the site of O = O bond formation in PSII caught by XFEL. Nature 543:131–135

Suga M, Akita F, Yamashita K, Nakajima Y, Ueno G, Li H, Yamane T, Hirata K, Umena Y, Yonekura S (2019) An oxyl/oxo mechanism for oxygen-oxygen coupling in PSII revealed by an x-ray free-electron laser. Science 366:334–338 (80-.)

Sugiura M, Inoue Y (1999) Highly purified thermo-stable oxygen-evolving photosystem II core complex from the thermophilic cyanobacterium Synechococcus elongatus having his-tagged CP43. Plant cell Physiol 40:1219–1231

Sugiura M, Rappaport F, Brettel K, Noguchi T, Rutherford AW, Boussac A (2004) Site-directed mutagenesis of Thermosynechococcus Elongatus photosystem II: the O2-evolving enzyme lacking the redox-active tyrosine D. Biochemistry 43:13549–13563

Suzuki H, Taguchi Y, Sugiura M, Boussac A, Noguchi T (2006) Structural perturbation of the carboxylate ligands to the manganese cluster upon Ca2+/Sr2 + exchange in the S-state cycle of photosynthetic oxygen evolution as studied by flash-induced FTIR difference spectroscopy. Biochemistry 45:13454–13464

Tso J, Sivaraja M, Dismukes GC (1991) Calcium limits substrate accessibility or reactivity at the manganese cluster in photosynthetic water oxidation. Biochemistry 30:4734–4739

Tsui EY, Agapie T (2013) Reduction potentials of heterometallic manganese–oxido cubane complexes modulated by redox-inactive metals. Proc Natl Acad Sci 110:10084–10088

Ugur I, Rutherford AW, Kaila VRI (2016) Redox-coupled substrate water reorganization in the active site of Photosystem II—The role of calcium in substrate water delivery. Biochim Biophys Acta (BBA)-Bioenergetics 1857:740–748

Umena Y, Kawakami K, Shen J-R, Kamiya N (2011) Crystal structure of oxygen-evolving photosystem II at a resolution of 1.9 Å. Nature 473:55–60

Vinyard DJ, Ananyev GM, Dismukes C, G (2013) Photosystem II: the reaction center of oxygenic photosynthesis. Annu Rev Biochem 82:577–606

Vogt L, Ertem MZ, Pal R, Brudvig GW, Batista VS (2015a) Computational insights on crystal structures of the oxygen-evolving complex of photosystem II with either Ca2 + or Ca2 + substituted by Sr2+. Biochemistry 54:820–825

Vogt L, Vinyard DJ, Khan S, Brudvig GW (2015b) Oxygen-evolving complex of Photosystem II: an analysis of second-shell residues and hydrogen-bonding networks. Curr Opin Chem Biol 25:152–158

Vrettos JS, Limburg J, Brudvig GW (2001) Mechanism of photosynthetic water oxidation: combining biophysical studies of photosystem II with inorganic model chemistry. Biochim Biophys Acta (BBA)-Bioenergetics 1503:229–245

Yachandra VK (1995) [26] X-Ray absorption spectroscopy and applications in structural biology. Methods in enzymology, vol 246. Elsevier, pp 638–675

Yamaguchi K, Miyagawa K, Shoji M, Isobe H, Kawakami T (2022) Elucidation of a multiple S3 intermediates model for water oxidation in the oxygen evolving complex of photosystem II. Calcium-assisted concerted OO bond formation. Chem Phys Lett 806:140042

Yano J, Yachandra V (2014) Mn4Ca cluster in photosynthesis: where and how water is oxidized to dioxygen. Chem Rev 114:4175–4205

Yano J, Kern J, Irrgang K-D, Latimer MJ, Bergmann U, Glatzel P, Pushkar Y, Biesiadka J, Loll B, Sauer K (2005a) X-ray damage to the Mn4Ca complex in single crystals of photosystem II: a case study for metalloprotein crystallography. Proc. Natl. Acad. Sci. 102, 12047–12052

Yano J, Pushkar Y, Glatzel P, Lewis A, Sauer K, Messinger J, Bergmann U, Yachandra V (2005b) High-resolution Mn EXAFS of the oxygen-evolving complex in photosystem II: structural implications for the Mn4Ca cluster. J Am Chem Soc 127:14974–14975

Yano J, Walker LM, Strickler MA, Yachandra VK, Debus RJ (2011) Altered structure of the Mn4Ca cluster in the oxygen-evolving complex of photosystem II by a histidine ligand mutation. J Biol Chem 286:9257–9267

Yao R, Li Y, Chen Y, Xu B, Chen C, Zhang C (2021) Rare-earth elements can structurally and energetically replace the calcium in a synthetic Mn4CaO4-cluster mimicking the oxygen-evolving center in photosynthesis. J Am Chem Soc 143:17360–17365

Yocum CF (2008) The calcium and chloride requirements of the O2 evolving complex. Coord Chem Rev 252:296–305

Zimmermann JL, Rutherford AW (1986) Electron paramagnetic resonance properties of the S2 state of the oxygen-evolving complex of photosystem II. Biochemistry 25:4609–4615

Zouni A, Witt H-T, Kern J, Fromme P, Krauss N, Saenger W, Orth P (2001) Crystal structure of photosystem II from Synechococcus elongatus at 3.8 Å resolution. Nature 409:739–743